

SCIENTIFIC AND TECHNICAL REPORT

FINAL TECHNICAL REPORT

MAY 17, 1995

Sponsored by

Advanced Research Projects Agency (DOD)

ARPA Order No. 5916 Amdt 68

Issued by U.S. Army Missile Command Under

Contract #DAAH01-94-C-R278

Applied Science and Technology, Inc.

35 Cabot Road, Woburn, MA 01801

Effective Date: July 20, 1994

Contract Expiration Date: February 20, 1995

Reporting Period: July 1994 - February 1995

P.I.: Barton Lane

Scientist: William Holber

Phone #: 617-933-5560

Title: "Plasma Processing

of Materials in

Microelectronics and

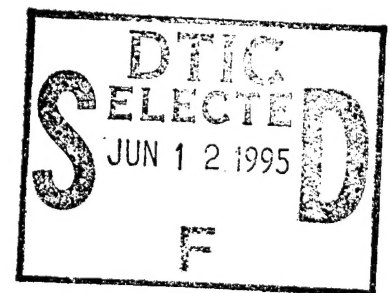
Photonics"

DISCLAIMER

"The views and conclusions contained in this document are those of the authors and should not be interpreted as representing the official policies, either express or implied, of the Advanced Research Projects Agency or the U.S. Government."

Distribution Statement:

Approved for Public Release: Distribution is Unlimited



DTIC QUALITY INSPECTED 3

19950608 072

Plasma Processing of Materials
in Microelectronics and Photonics

Contract #: DAAH01-94-C-R278

issued by:

U.S. Army Missile Command
Redstone Arsenal, Al 35898

Final Report - Phase I Technical Program

May, 1995

Introduction

Accession For	
NTIS CRA&I	<input checked="" type="checkbox"/>
DTIC TAB	<input type="checkbox"/>
Unannounced	<input type="checkbox"/>
Justification	
By	
Distribution /	
Availability Codes	
Dist	Avail and/or Special
A-1	

Goals of Program

The goal of the project is to develop a process for the patterning of SiN_x films over $GaAs$ which maintains sub-micron line shape while minimizing damage to the $GaAs$ crystal substrate. The development activities are being pursued using an ECR source to provide a high density plasma and an RF powered substrate holder to provide the ion energy and directionality. The chemistry chosen is CF_4/O_2 buffered with Argon.

The goals of the Phase I program are to develop an understanding of the key physical processes which determine etch line shape, damage to the $GaAs$ crystal substrate and etch radial uniformity through an integrated experimental and modelling program. Based on this understanding a new process and reactor hardware set and diagnostics will be developed; the development and construction of this new process-hardware-diagnostic set would be undertaken in Phase II.

Target Application

The extension of HEMT performance to millimeter wave frequencies requires the use of low resistance sub $0.25 \mu m$ gates. One method for achieving shorter gate lengths is the dielectric assisted T-gate process in which the gate length is defined in a SiN_x layer. In this process the e-beam lithography step has been optimized for achieving the desired gate length. An etch process that faithfully replicates e-beam defined resist openings in the SiN_x layer without introducing damage to the underlying III-V substrate is required to fabricate sub-micron T-gates.

Summary of Findings of Phase I

For the parameter regime characterized by:

- high plasma density,
- low bias voltage,
- low neutral density,
- a chemistry selective for etching SiN_x over $GaAs$,

the following results were obtained:

- * line shape is determined primarily by the wafer DC bias voltage and hence ion energy;
- * etch rate depends on ion current and wafer DC bias
- * damage to the underlying substrate scales primarily with ion current and only weakly with ion energy

* damage increases with dose up to a saturation value. The saturation value depends on ion current.

The relative independence of damage on ion energy was completely unexpected since in RIE systems where the ion energy is typically much higher, damage scales with ion energy. This finding permitted the identification and experimental verification of an optimized process point which yields high rates, good lineshapes and low damage. This process point could be significantly improved by employing a real-time sensor based control system to implement a multi-step process.

The simulations in Phase I have provided an insight into the fundamental processes determining the radial uniformity of ion flux to the wafer and into the process of activation of the feed stock gases through electron impact dissociation and loss of reactants through wall recombination. It was found that the radial uniformity of the ion flux was determined by both the microwave power deposition profile and the nature of the electrical properties of the material surfaces on which field lines terminate. The microwave deposition power can be altered by modifying the microwave launch structure and the internal material surfaces can be actively biased to influence the ion radial flux uniformity.

Status of Project

The Phase I research phase has provided a concrete set of process conditions which can be used with the current reactor hardware to permit rapid, low damage etching of vertical sidewall sub-micron features in *SiN* over *GaAs*. In addition the Phase I research phase has provided significant and unexpected insights into the nature of the damage mechanism and into the processes determining the plasma and neutral processes in the reactor. This underlying fundamental knowledge is being used to redesign the current reactor to permit more rapid, damage free etching of *SiN* overlayers.

This redesign of the reactor involves both changes to the hardware set to permit more radial uniformity of ion current and control of relative radical species concentrations and the integration of a real-time sensor based control system. This latter will permit the implementation of a multi-step process which will minimize the damage caused during the crucial phase when the *SiN* overlayer etch nears end point.

Background

Motivation for use of ECR

Plasmas generated by electron cyclotron resonance (ECR) are attractive because the plasma source and substrate DC bias can be decoupled and independently optimized to obtain a high resolution etch processes while minimizing damage to the underlying substrate. Even with no RF bias it is possible to deliver a high current density (10.0 mA/cm^2) with an energy determined by the sheath potentials of 10-30 eV at low neutral pressures. It has been reported¹⁻⁷ that dry etching with an ECR reactor results in less plasma induced damage compared to conventional reactive ion etching. Therefore considerable interest has been shown in the use of ECR sources for sub micron, low damage dry etching. In particular, there are numerous papers in the literature that report on low damage ECR etching of *GaAs*.^{3,8,9} Cheung et. al.⁸ demonstrated that very little damage is caused by ECR etching of *GaAs* using $\text{CCl}_2\text{F}_2/\text{He}$ as the etch gas. Ko et. al.¹⁰ have reported that damage was reduced with low ion energy and concentration of reactive species while etching *GaAs* in an ECR with Cl_2/N_2 plasma. Constantine et al.³ have reported on the low damage ECR etching of *GaAs*, *InP*, *InGaAs* and *AlInAs* with methane based gases. Others have reported on low damage, anisotropic etching of silicon. These studies have involved etching of doped *GaAs* in which an equilibrium is established between the creation of damage and the removal of the damaged layer by etching. However, limited information is available on low damage, sub micron, selective, ECR plasma etching of *SiN_x* films deposited on *GaAs*; in this case the reactive working radicals react with the *GaAs* crystal to form non-volatile products and the etching is due solely to physical sputtering.

Experimental Apparatus and Method

Experimental Summary

A Plasma Quest model 357-IV electron cyclotron resonance reactor was used for this study shown schematically in Figure (1). The Plasma Quest reactor incorporates an ASTeX low profile ECR source which is powered by a 1000 watt, 2.45 GHz power supply. A source (upper) electromagnet is used to generate an axial magnetic field along which microwaves are launched through a dielectric window located within the magnet bore. The microwave electromagnetic fields are resonant with the electron gyromotion at a point a few centimeters from the dielectric window. This resonance which permits an efficient transfer of energy to electrons on each pass through the resonance, together with strong reduction in radial (cross-field) electron transport, permits high density ($1.0 \times 10^{12} \text{ cm}^{-3}$) plasmas to be sustained at pressures between 0.5 and 10.0 mtorr. An additional electromagnet mounted at the level of the wafer chuck can be used to collimate the magnetic field to the wafer processing plane; this magnetic was not used during these experiments.

The plasma source is mounted on 16 " ID cylindrical aluminum multipole magnetic bucket. The bucket consists of 20 vertical rows of permanent magnets with a magnetic field strength just inside the bucket wall of approximately 1 kG; this field drops rapidly into the interior. The multipoles have been found to increase plasma radial uniformity over large areas and to increase ion density at large source-substrate separations. The interior surface of the multipole bucket is anodized and was measured to have a high resistance to ground in atmosphere. The top plate containing the microwave window assembly is fabricated from stainless steel and had a low resistance to ground in atmosphere.

The aluminum multipole bucket is mounted on a stainless steel lower cylindrical chamber which provides ports the vacuum pump and the wafer load lock. A 2200 liter/sec turbomolecular pump is used to provide an ultimate chamber pressure of 10^{-8} torr. The 16 inch inner diameter reactor chamber is capable of uniformly processing up to 8.0 inch wafers although 3.0 inch wafers were used for this study. A vacuum load lock is used to minimize the exposure of the reactor to atmospheric ambient. The cylindrical vacuum chamber below the multipole bucket is also stainless. The top plate and lower stainless steel chamber provide the ground reference for the plasma.

The chuck assembly consists of an RF powered chuck body, a stainless steel annular hold down ring which holds the wafer against an insulating O ring seal and a closely fitting dark space shield. The volume between the wafer backside and the chuck top surface which is anodized aluminum is filled with helium to provide thermal contact with the chuck body which is thermally controlled via an external chiller. The substrate chuck is powered by an 300 watt 13.56 MHz RF generator through a blocking capacitor located in the matching network. The chuck body is surrounded by an anodized aluminum dark space shield whose conducting aluminum core is grounded.

The wafer and the stainless steel hold down ring are separated from the chuck body by an insulating O ring and an anodized aluminum layer and therefore do not make electrical contact with the chuck body. The chuck body is itself isolated from ground by the blocking capacitor and contacts the plasma primarily through the gap between the top of the dark space shield and the bottom of the wafer hold down ring. The DC potential of the chuck body is sensed as a diagnostic but is not necessarily the same as the DC bias of the wafer and hold down ring assembly. The chuck height can be adjusted and for these experiments was placed at 12.5 and 9.5 inches below the top stainless steel over of the multipole bucket.

Statistical Designed Experiments

Designed experiments were performed in order to optimize the etching of SiN_x in a $\text{CF}_4/\text{O}_2/\text{Ar}$ plasma. These experiments were performed to optimize the process with regard to the following response variables: (listed in order of importance) damage to the underlying GaAs layer, sidewall profile (anisotropy), selectivity to photoresist, uniformity and SiN_x etch rate.

Sample Preparation

Samples used for the damage study consisted of a 300 - 500 nm thick epitaxial grown GaAs layers,

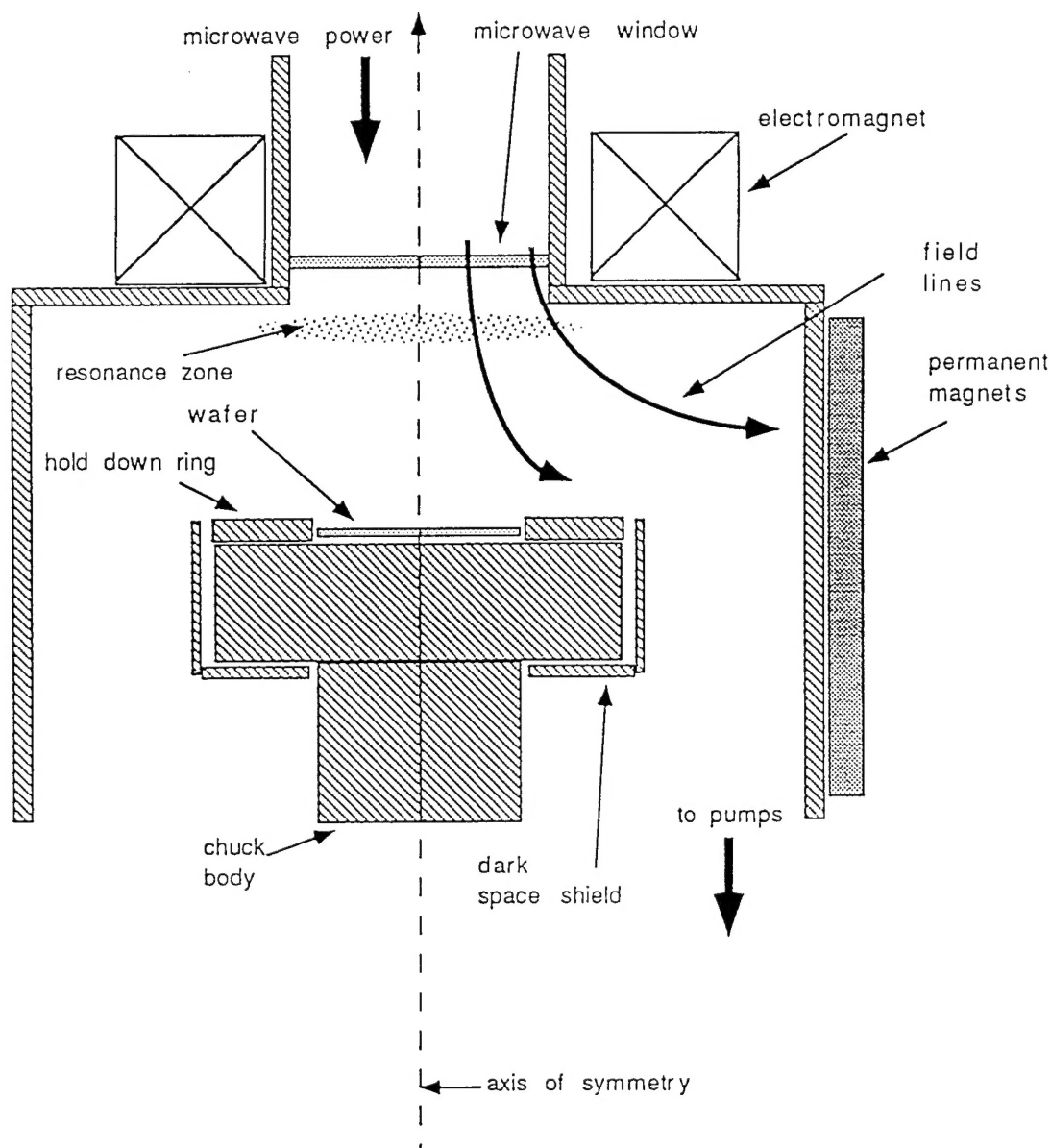


Figure (1.0). Schematic of reactor used for experiments. Microwave power is injected from above through a dielectric window. A single electromagnet provides a dipolar main field which establishes the ECR resonances zone. The chuck is powered by RF through a blocking capacitor.

doped with silicon to $1.0 \times 10^{17} \text{ cm}^{-3}$. Damage test samples were exposed to the plasma for 60.0 seconds. Damage was measured by the change in sheet carrier concentration ($\Delta N_s = N_s(\text{controlsample}) - N_s(\text{damagetestsample})$), which was obtained by Polaron measurements. Samples used to study sidewall profile (anisotropy), selectivity to photoresist, uniformity and SiN_x etch rate, consisted of 500 nm thick SiN_x PECVD layer, on top of a 3.0 inch GaAs substrate. The SiN_x layer was patterned with 1.8 μm of positive resist. Sidewall profile (anisotropy) was determined by rating SEM photos after the samples were etched. For the purpose of comparison, all samples were etched until $\approx 100 \text{ nm}$ of SiN_x remained on the sample. Etch profile was ranked 1 (optimal) to 10 (least desirable). Selectivity to photoresist and SiN_x etch rate were determined from 12 point, before and after thickness measurements of the SiN_x and resist taken from a Nanometrics 210 film thickness system. Selectivity was determined by dividing the etch rate of the SiN_x

by the etch rate of the resist. Uniformity was calculated by taking the difference between the before and after thickness measurements of the SiN_x , calculating the average and dividing by the standard deviation.

Langmuir probe measurements

Langmuir probe measurements were conducted, to determine if a correlation existed between the process results and the plasma parameters. A tungsten Langmuir probe tip with an estimated collection area of 0.0741 cm^2 was used. Radial ion saturation current was measured at a constant probe bias of -90 V . The probe was positioned approximately 3 inches above the substrate plane. Probe I-V traces were taken on axis and at a radius of $3''$.

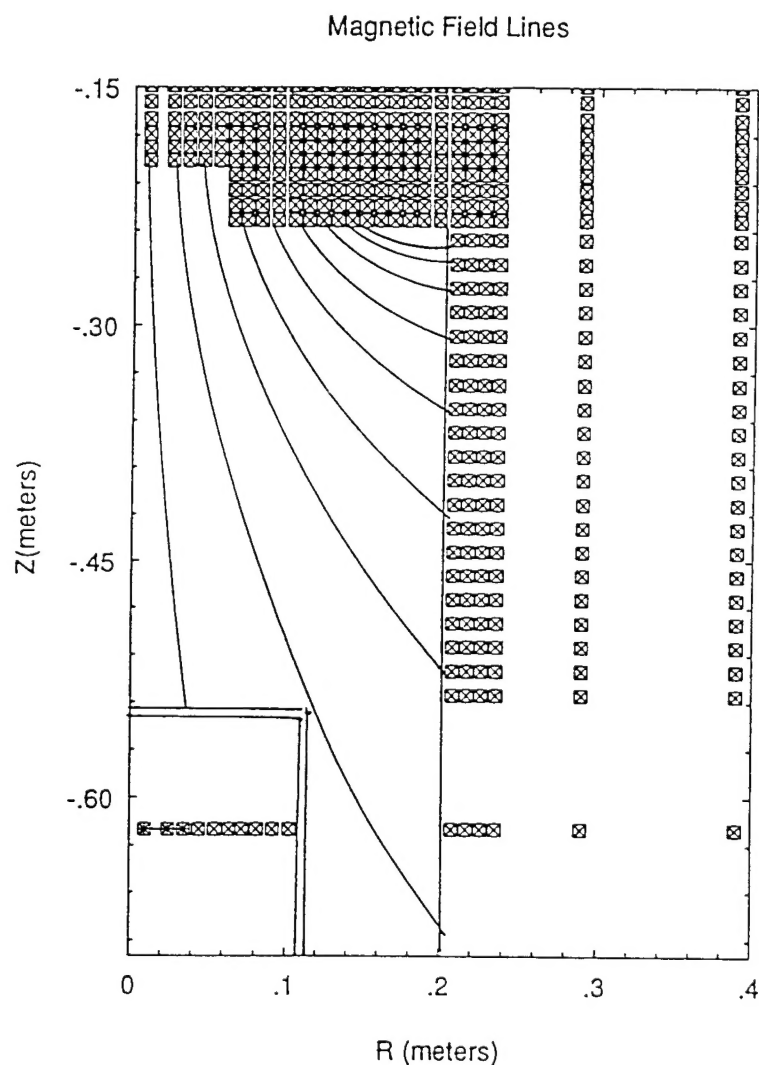


Figure (1.1). Magnetic field lines for reactor. Note that chuck maps into small radius at microwave window.

Experimental Results

Initial screening

Due to the large number of control parameters (9), an initial screening experiment was performed. An orthogonal array, OA16, based on a technique developed by Professor Taguchi, was implemented for the initial experiment. This initial design of experiments (DOE) established which control parameters had the most effect on the given response variables as well as determine the settings for the next DOE. Table (1.) lists the 9 control parameters with corresponding low and high settings and results for this initial screening experiment.

OA16 parameter settings and results

Control Parameters	Low Setting	High Setting	Effects on variables
1) Chuck Height (inch)	2.0	9.0	large effects
2) Microwave (Watts)	400	1000	large effects
3) RF Power (Watts)	0	300	large effects
4) Total Flow (sccm)	26	78	large effects
5) Chamber Pressure (mTorr)	1	20	large effects
6) Upper Magnet (Amps)	145	185	no significant effect
7) Lower Magnet (Amps)	-10	+10	no significant effect
8) O ₂ %	4	10	selectivity and uniformity only
9) Chuck Temperature (°C)	-5	25	-5° C resulted in good sidewall profile

Table (1.) - Control parameters and responses for initial screening study.

Variation in the source (upper magnet) and substrate magnetic fields (lower magnet) did not have any significant effect on any of the response variables over the ranges studied. Therefore the upper and lower magnets were fixed at 185 and 0 amps, respectively, for the next experiment. Selectivity was found to improve slightly at the low O₂ setting (4.0%) while uniformity improved slightly at the high O₂ setting (10.0 %). However, because the O₂ concentration had no significant effect on damage or anisotropy, the O₂ was set at 7.0% for the next experiment. In the context of RIE etching SiO₂ over Si there is data to suggest that increased O₂ concentration suppresses the formation of CF fluorocarbon polymers while decreasing the selectivity of oxide over silicon. The lack of dependence of anisotropy on oxygen concentration suggests that the anisotropy does not originate from fluorocarbon sidewall passivation.

The low chuck temperature resulted in good sidewall profile therefore the chuck temperature was set at -5° C for the following experiment. The improvement in sidewall profiles with chuck temperature is indicative of an isotropic chemical etching which exhibits an activation energy barrier. Since SiN is known to be etched by F without ion bombardment, we assume that this is the process at work here. Chuck height, microwave power, RF power, total flow, and chamber pressure all had various large effects on the response variables. Table (1.) lists the 9 control parameters with corresponding low and high settings as well as the

results for this initial experiment.

Two level-five control parameter DOE

A 2^{5-1} fractional factorial designed experiment was performed, to study the potential for possible interaction between the 5 remaining control parameters (Chuck height, microwave power, RF power, total flow and chamber pressure); upper magnet, lower magnet, O_2 ratio (O_2 sccm/total flow sccm) and base plate temperature were fixed for this experiment. This experiment was selected in order to optimize the response variables previously mentions, indicate major trends, and determine the direction for future experimentation. Table (2.) highlights the run conditions for the 2^{5-1} fractional factorial experiment. Main and interaction effects were calculated and plotted.

Run conditions For 2^{5-1} Fractional Factorial Designed Experiment

<u>Control Parameters</u>	<u>Low Setting</u>	<u>High Setting</u>
1) Chuck Height (inch)	4.0	7.0
2) Microwave (Watts)	500	800
3) RF Power (Watts)	10	50
4) Total Flow (sccm)	26	78
5) Chamber Pressure (mTorr)	2	10

<u>Control Parameters</u>	<u>Fixed Settings</u>
6) Upper Magnet (Amps)	185
7) Lower Magnet (Amps)	0
8) O_2 %	7
9) Chuck Temperature ($^{\circ}C$)	-5

Table (2.) - Run conditions for main fractional factorial designed experiment.

Damage

The experiments indicated that chamber pressure had the most effect on damage to the underlying GaAs layer. Figure (2) shows that damage decreased as chamber pressure increased (error bars show the standard error mean for the high and low settings).

sidewall profile (anisotropy)

RF power had by far the largest effect on the anisotropy. SEM photos and the graph in figure (3) indicate that RF power is necessary for vertical sidewalls.

radial uniformity

Radial uniformity improved with RF power, decreasing chuck height, low microwave power and high total flow as shown in Figure (4). As we shall see below, high microwave powers lead in general to more hollow ion current profiles and thus to less uniformity.

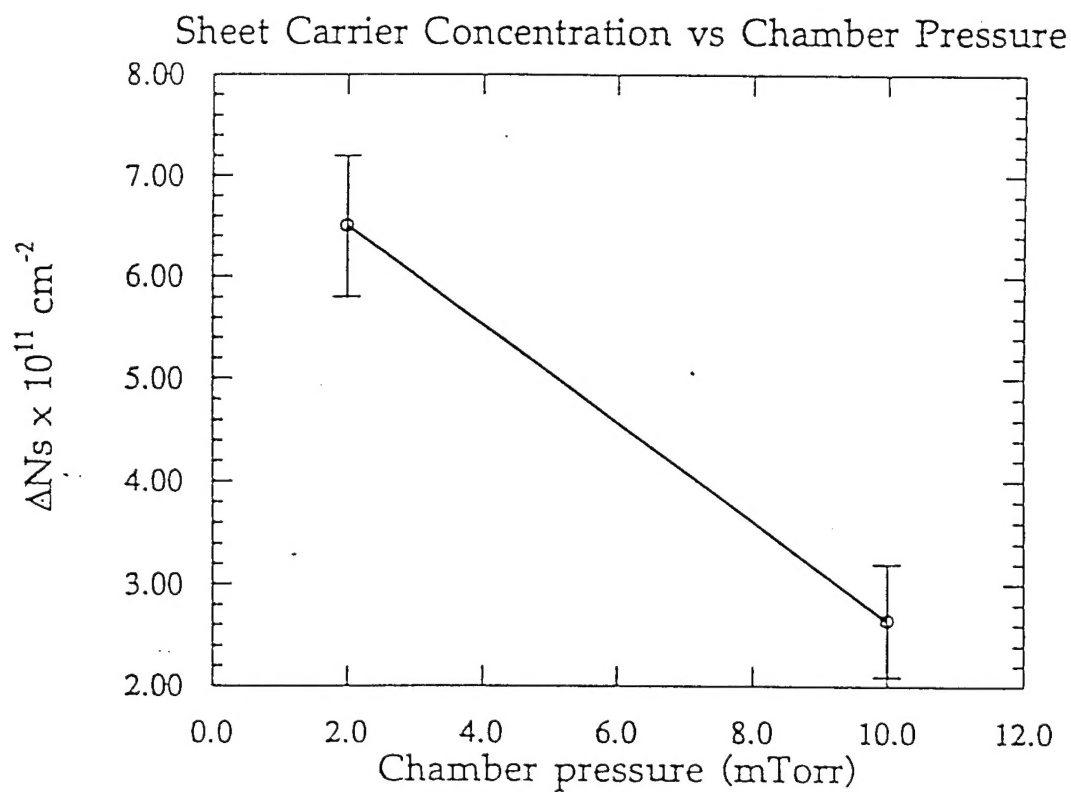


Figure (2) - Change in sheet carrier concentration as a function of chamber pressure.

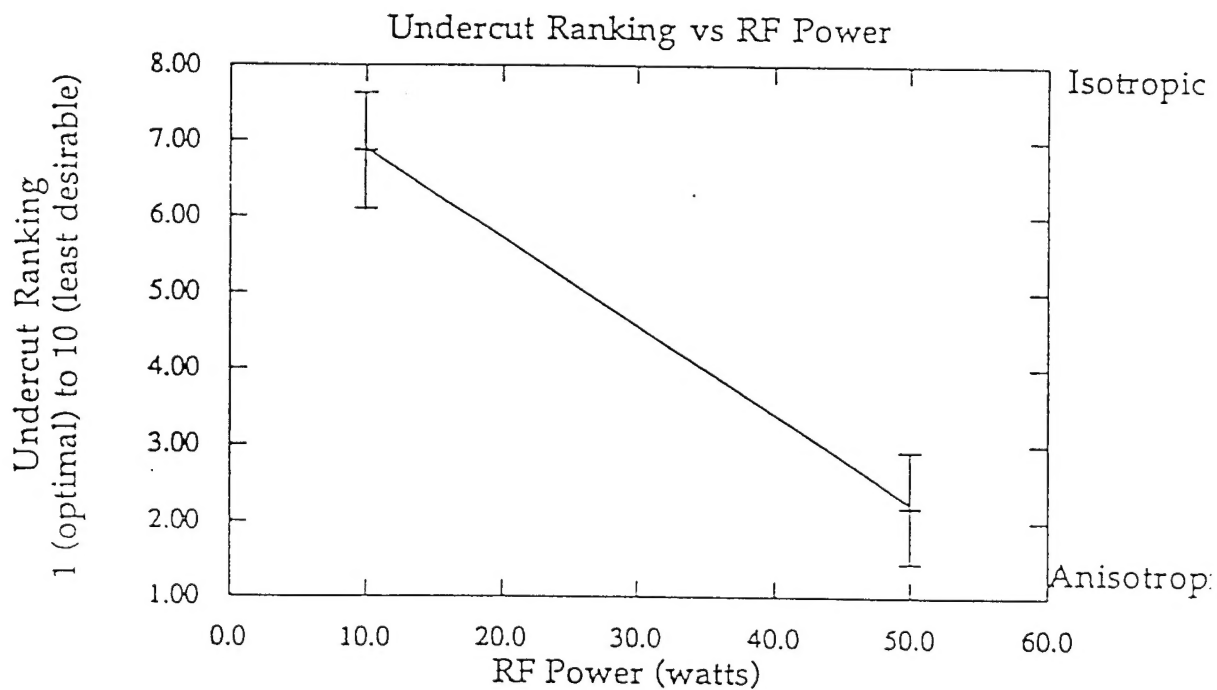


Figure (3) - Undercut ranking versus RF power.

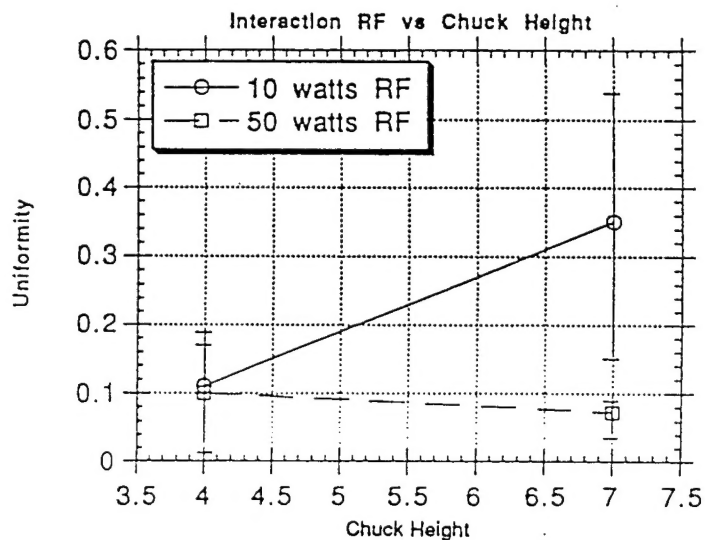


Figure (4.a) - Uniformity as function of chuck height for two RF powers.

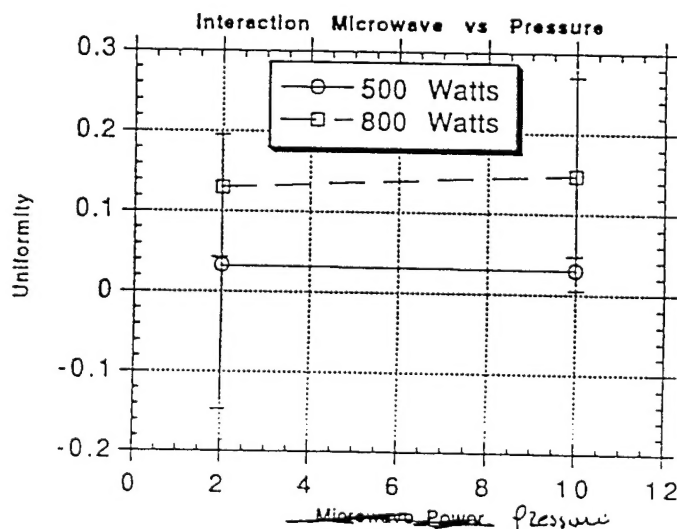


Figure (4.b) - Uniformity as a function of pressure for two microwave powers.

SiN_x etch rate

SiN_x etch rate scaled positively with RF power and total flow and negatively with chamber pressure as shown in Figure (5). The scaling of the SiN_x etch rate with current does not emerge cleanly from the data. Shown in Figure (5.d) is a scatter plot of etch rate versus ion saturation current measured on axis for the entire data set; the scatter in the data suggests that other control parameters dominate the etch behaviour. However, the fact that the etch rate clearly scales with RF power indicates that it is an ion driven process

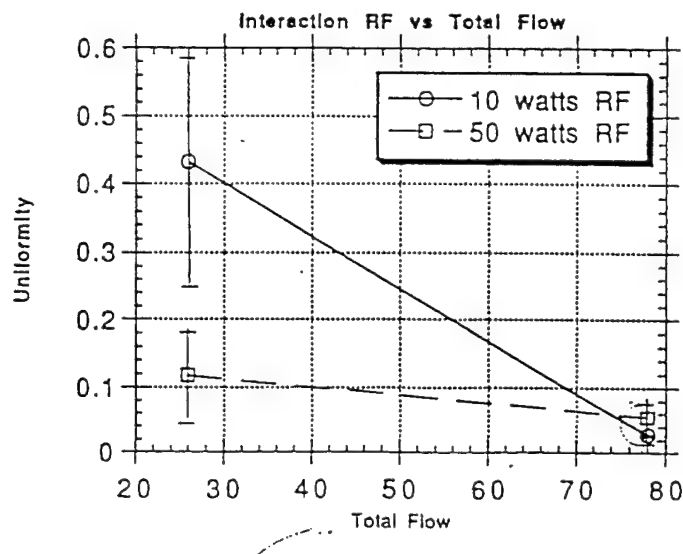


Figure (4.c) - Uniformity as a function of total flow for two RF powers.

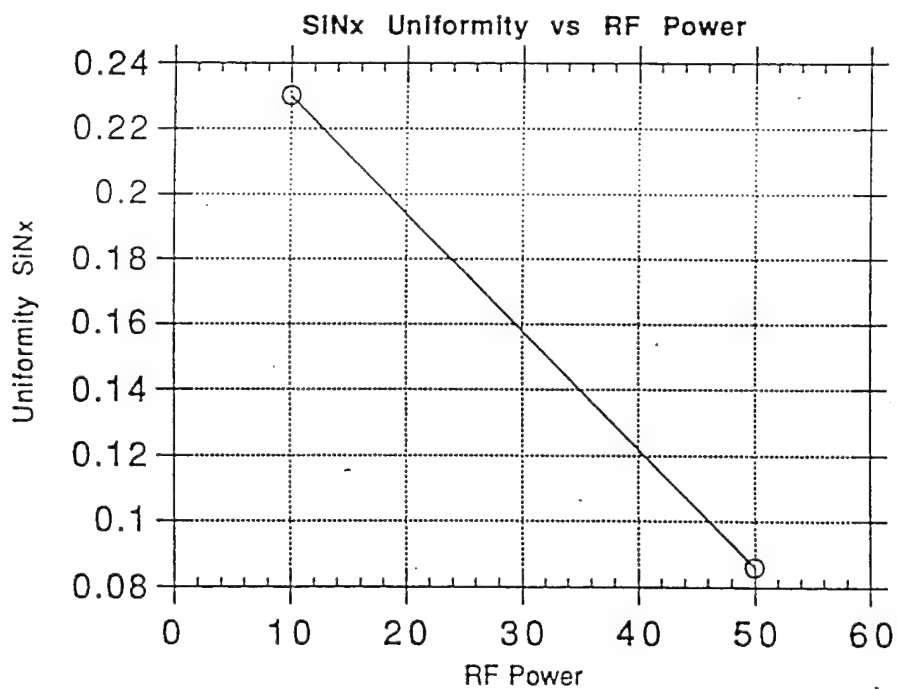


Figure (4.d) - Uniformity as a function of RF power with all other variables averaged.

and therefore dependent on the availability of ions. However, for a given RF power, an increase in the ion current density requires a decrease in the ion energy. This is consistent with an etch rate dependence on the total ion power flux (current \times potential drop) to the wafer, which would be independent of ion current.

Note that there is an etch rate dependence on total flow. This is consistent with the depletion of the reactive species. The implications of this are considered below.

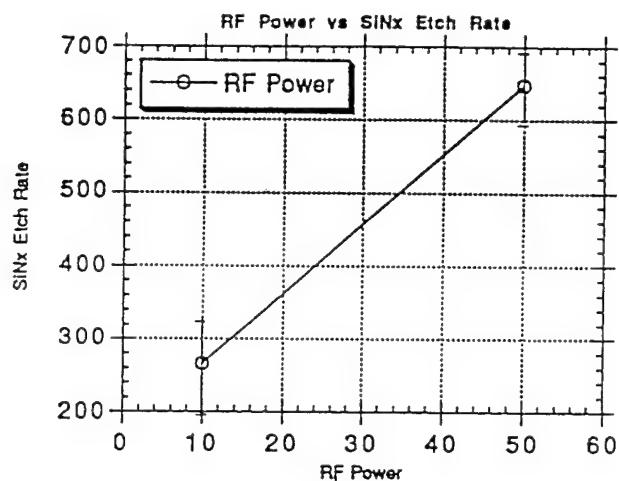


Figure (5.a) - Etch rate as function of RF power.

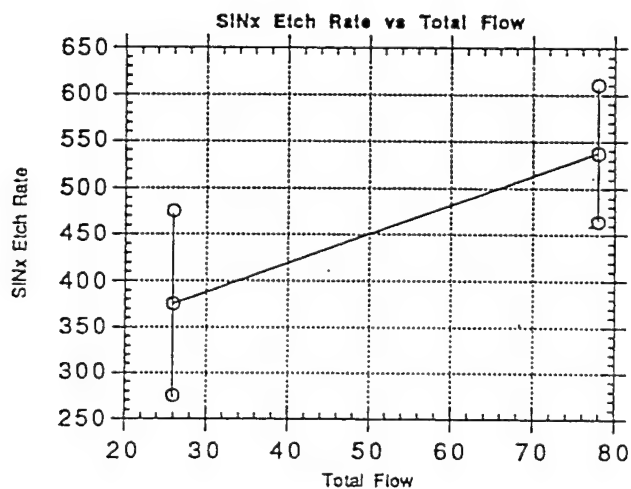


Figure (5.b) - Etch rate as function of total flow.

Correlation of process results with Langmuir probe data

In order to correlate the process results with the plasma parameters Langmuir probe scans were performed which duplicated the runs of the 2⁵-1 fractional designed experiment. After reviewing the radial ion saturation current profile data, it was found that ion saturation current increased with decreasing chamber pressure as is shown in Figure (6). This is similar to the findings of the 2⁵-1 fractional experiment where damage increased as chamber pressure decreased (Figure (2)). A plot of ion saturation current versus ΔN_s

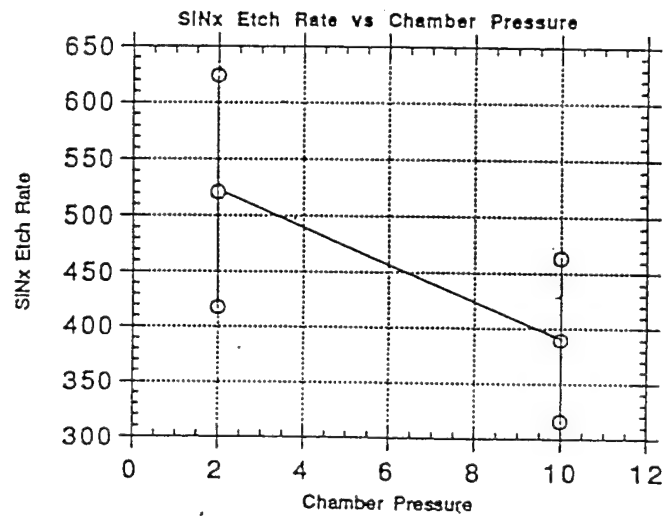


Figure (5.c) - Etch rate as function of chamber pressure.

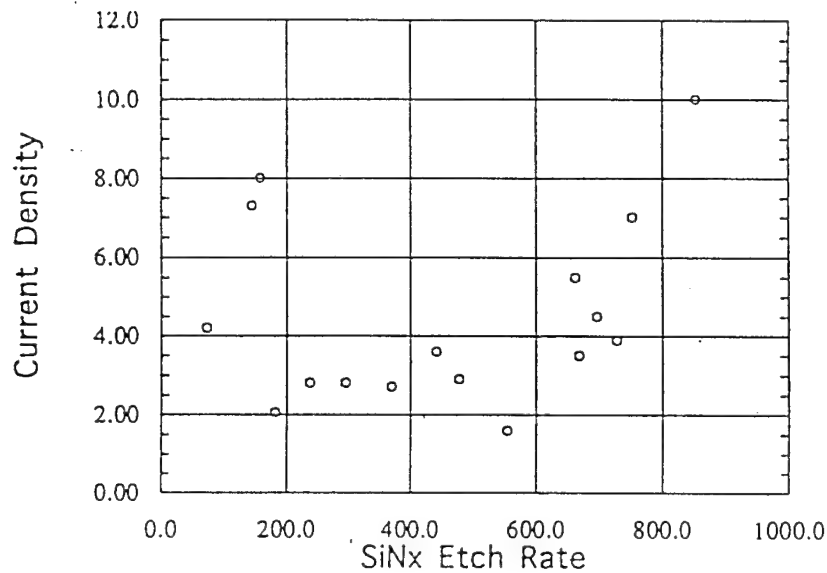


Figure (5.d) - Etch rate as function of ion current density.

(Figure (7)) revealed that damage was strongly correlated with ion current density. The correlation between damage and ion current density has been reported by others; Gadgil et. al.⁷ reported that damage to silicon MOS devices increased with increasing ion current density. Hara et. al.⁹ reported a similar observation when *GaAs* damage test samples were exposed to an ECR SF_6 plasma. These papers did not present a model for the damage mechanisms at work. We present below a hypothesis for the damage mechanism.

No dependence of damage on the wafer RF bias (ion energy) was found for the 2⁵-1 experiment. This

is shown in the Figure (8) which plots change in sheet carrier concentration as function of RF power for two different total flow rates. The higher flow rate shows virtually no dependence on of damage on RF power, while the lower flow shows a weak dependence as compared to the dependence on ion current. These results suggest that ion flux not ion energy plays the major role in introducing damage (within this bias range) to the $GaAs$ layer after removal of the SiN_x . This was a very significant and unexpected result.

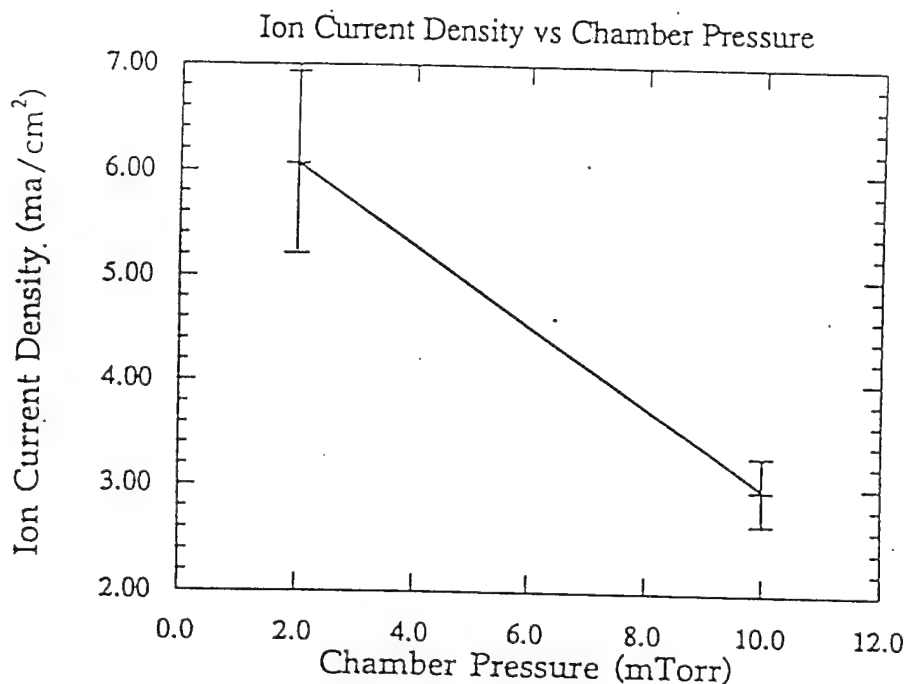


Figure (6) - Langmuir probe ion saturation current versus chamber pressure.

Additional damage related experiments

dose

To further examine the dependence between damage and plasma parameters a series of experiments were performed. Damage dose dependence was investigated by duplicating damage experiments at varying ion saturation current levels and times. Figure (9) shows that by increasing the length of time a damage test sample is exposed to the plasma, (at various ion saturation levels), the level of damage increases initially but then saturates. Similar results have been observed for reactive ion etching of SiO_2 over $GaAs$ by Seaward et. al.¹¹ Saturation of damage after extended exposure to the plasma was explained there by the total depletion of carriers in the layer due to the introduction of deep acceptor levels. However, since the damage saturation level increases with increasing ion current density, the current results indicate that the saturation our results do not indicate such a total depletion of carriers at least for the lower current densities. There is also evidence in the work of Seaward et al.¹¹ that the damage is introduced very early in the exposure time. The results presented here did not resolve the early time dependence of the damage in detail; such experiments will be part of the Phase II effort.

Refinement of damage-ion energy experiments

Experiments were also performed in order to further investigate the relationship between ion energy and damage. Conditions used for the dose dependence experiments, were repeated for the ion energy investigation, however, the RF power was varied between 0 and 300 W. Figure (10) shows that damage increases with

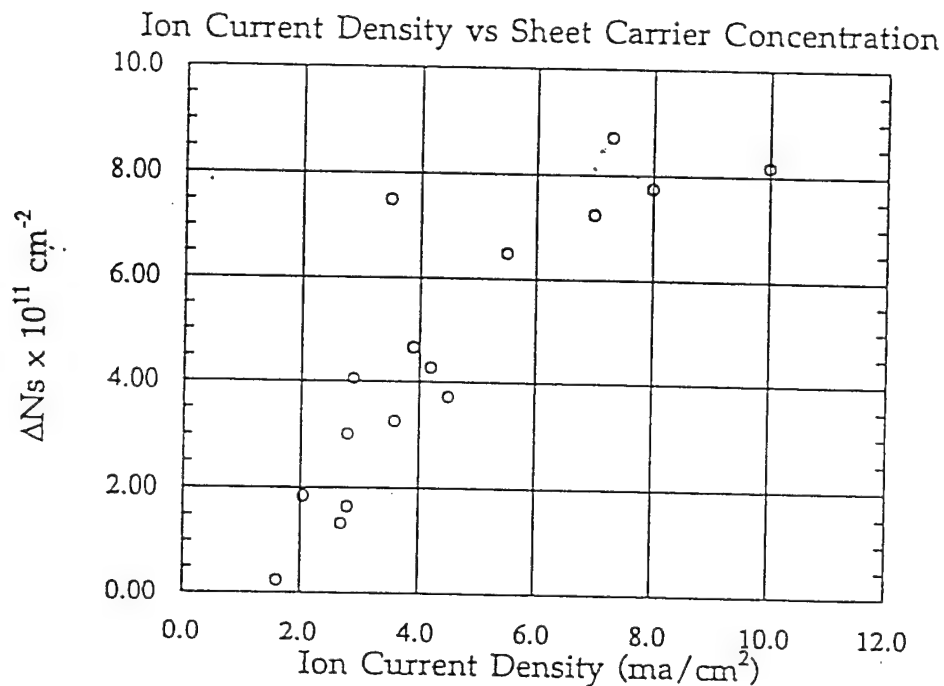


Figure (7) - Change in sheet carrier concentration versus ion current density.

increasing ion current density and, above 100 V, with bias, (not examined in the design of experiments). Operating conditions with 1.6 mA/cm² ion current density and below -150 V DC bias showed very low levels of damage.

Optimized process point

Since sidewall anisotropy was found to depend on RF bias while damage was found to depend on ion saturation current, it is possible to find an optimal process point at which both are maximized. A confirmation experiment was conducted to verify this process point. Figure (11) shows an optimized sidewall of a sample etched at 500 watts microwave power, 100 watts RF power, 78 sccm total flow, 4 inch chuck height, 7% O₂, upper magnet current of 185 amps, lower magnet current of 0 amps, -5° C chuck temperature and 10.0 mtorr chamber pressure. This optimized sample had a relatively low level of damage ($\Delta N_s = -0.77 \times 10^{11} \text{ cm}^{-2}$), ion current density of 1.6 mA/cm², selectivity of 1.4, uniformity of 2% across a 3" wafer and a SiN_x etch rate of 784 Angstroms/min.

Model for Damage Mechanism

We first summarize the experimental results related to damage:

- Damage increases with ion current
- Damage is weakly dependent on RF bias for bias below 100 V.
- Damage saturates with dose with a saturation level which is current dependent

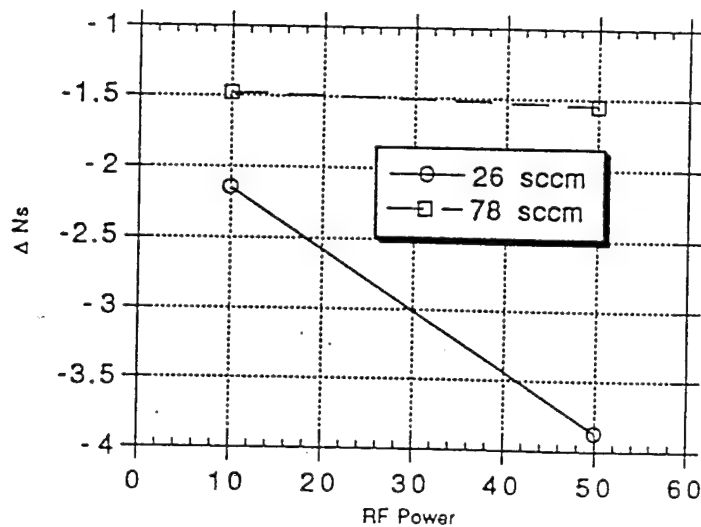


Figure (8) - Change in sheet carrier concentration versus RF power to chuck for two total flow rates.

- Damage is not strongly affected by the oxygen content
- The damage as evidenced by the Polaron curves extends 500-1500 Angstroms into the surface, far below the ion penetration depth at energies below 100 V.

The model we present has the following elements:

1. Damage occurs primarily due to ion channeling explaining the relatively large depth of the damage. This is consistent with the deep extent of the damage and with previously reported results¹² that damage scales inversely with ion mass.
2. Damage occurs during the first exposure of the *GaAs* crystal when the channeling paths are open
3. An amorphous surface layer develops as plasma exposure continues which blocks the penetration of ions deep into the interior and limits damage to the upper 50 Angstroms over which the carrier depletion is essentially complete.
4. The time to build up this overlayer and its ultimate thickness depend on the ratio of ion to neutral fluxes which increases with increasing ion flux and decreasing pressure
5. The overlayer consists primarily of *GaF₃* species and not fluorocarbon polymers since oxygen plays little role in affecting damage.

No direct experimental evidence of such a *GaF₃* overlayer was obtained in the present set of experiments; however, Seaward et al.¹¹ characterized such a layer for an RIE system etching *SiO₂* over *GaAs*. They found the layer to be 20 Angstroms thick and to consist of *GaAs* for a *CF₄/O₂* chemistry in an RIE reactor; note that their bias voltages were larger than those in the present study.

Evidence that a protective overlayer forms is also consistent with the results of Pang¹² who found that

ΔN_s vs exposure time as a function of ion current density

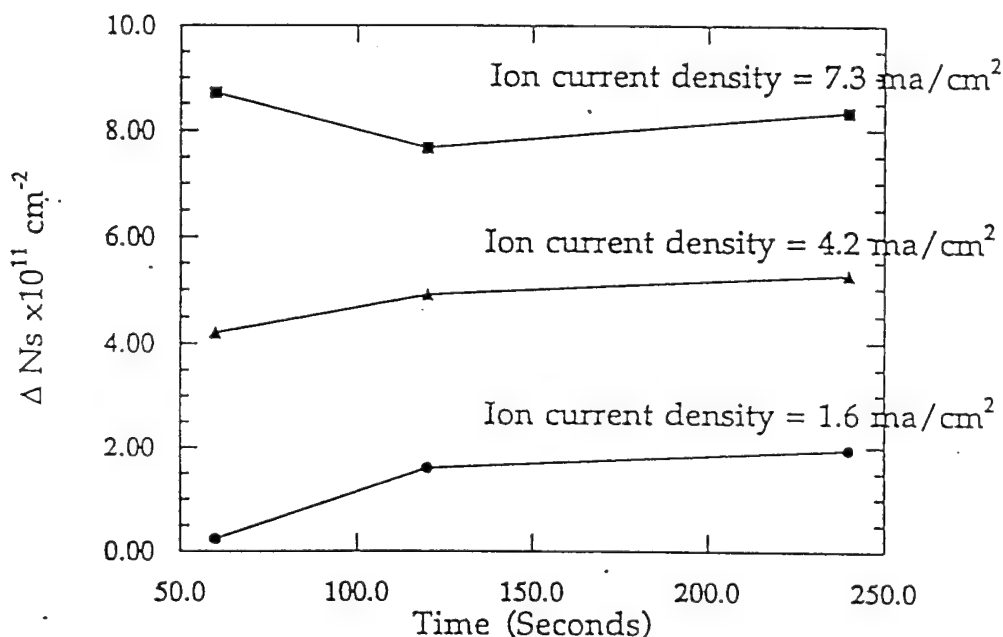


Figure (9) - Damage as a function of dose for three ion saturation current densities 1.6, 4.2 and 7.3 mA/cm².

reactive gases such as CF_4 produced less damage than pure argon. Note that this is not due to an increased removal rate of the damaged surface since etching in CF_4 proceeded at slower etch rate than pure argon.¹²

The weak dependence of damage on RF bias which was observed in the experiments performed here requires that for ion energies up to some threshold:

- the overlayer protects the underlying substrate completely from ion damage
- the thickness of the overlayer is independent of ion energy.

For the bias voltages in the present study (< 100 V), the ion penetration depth is less than 50 Angstroms which is comparable to the layer thickness found by Seaward et al.¹¹. Thus the overlayer, once formed, could have afforded complete protection independent of ion energy up to some threshold.

The independence of overlayer thickness from RF power for a given ion current density requires a competition in film formation processes. One possible hypothesis is that neutral atomic F is adsorbed the surface which is then bombarded by ions. The ions can either (a.) sputter moieties such as GaF_x from the surface, (b.) aid in the penetration of atomic F to deeper layers by mixing of the surface atoms, and (c.) deposit a layer on the surface. At low energies, these processes may balance each other leading to a relative insensitivity to ion energy.

The formation of a protective overlayer, however, requires a sufficient flux of atomic F relative to non-depositing ions which will thin the layer. The fact that the etch rate of SiN_x , which mostly likely scales with atomic F concentration, depends on total throughput, suggests that the atomic F both the etch process and protective layer formation process are limited by the availability of F . If this is the case then ion current densities of non-depositing species which are in excess of the flux of atomic F will thin the layer rather than promoting deposition or mixing. This is also consistent with the data shown in Figure (8) in which the

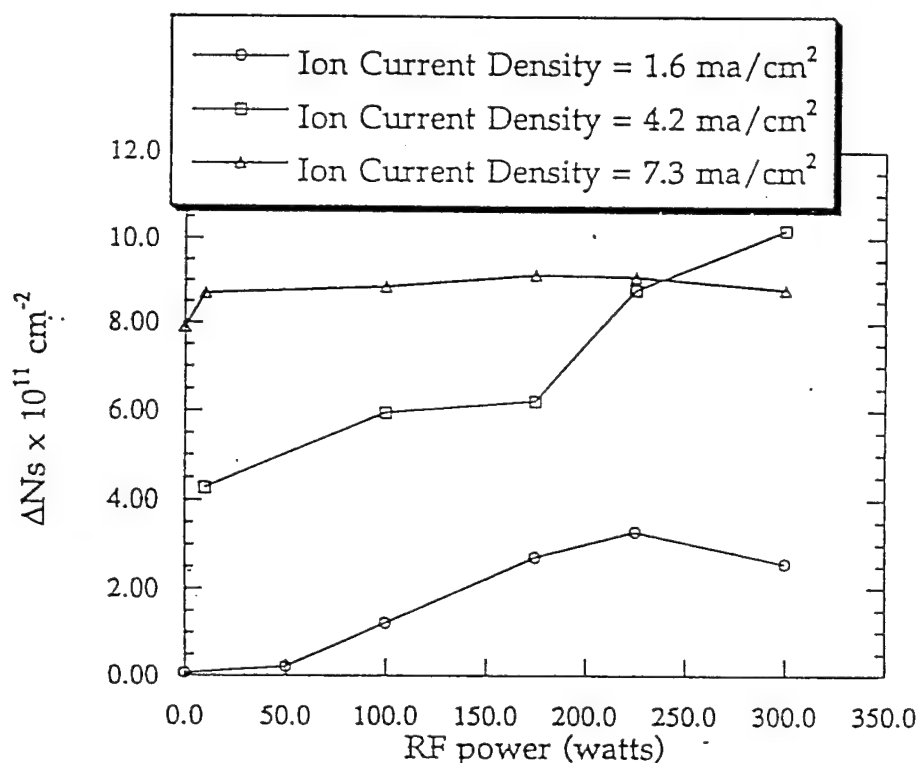


Figure (10) - Change in carrier sheet concentration as a function of RF power for three different ion saturation currents.

high flow rate shows virtually no dependence on RF power, while the lower flow rate shows a dependence of damage on RF power.

An example of such ion aided deposition was studied by Oehrlein¹³ in the context of SiO_2 etching by a CF_4 chemistry in an ECR source. Oehrlein's group found that at low energies, there was in fact a net deposition of a fluorocarbon film due to ion bombardment. We note this example solely to indicate ions can play a more complex role in overlayer formation than simple sputtering of species from the surface. We show a graph of from this group's work in Figure (12) indicating ion deposition of a fluorocarbon layer at low ion energies and the disappear of this layer at higher energies accompanied by an etching of the underlying SiO_2 .

Note that in purely etching chemistries such as noble gas or Cl_2/N_2 mixtures, no overlayer forms and damage is proportional to ion energy¹⁰ even in an ECR sources where bias voltages can be of order or less than 100 V. For such chemistries the final damage is the result of balancing damage formation through ion impingement with removal of the damaged surface through the formation of volatile by-products. An entirely different picture emerges for a non-etching chemistry such as $\text{CF}_4/\text{O}_2/\text{Ar}$. For such a chemistry in which the surface reaction by-products are non-volatile, the dynamics of the protective overlayer formation are crucial to the preventing damage in the low bias voltage, high current density regime.

Numerical simulation method

Goals and summary of the simulation findings

The goal of the simulations is to shed light on the underlying physics related to the plasma generation and transport and the neutral chemistry which is initiated by electron impact dissociation. The process of comparing the simulations to experimental results has led to forming an in-depth understanding of many of the processes at work in the reactor.



Figure (11) - SEM of optimum sidewall profile for sample etched at 100 W RF, 78 sccm total flow, 4 inch chuck height, 7% oxygen, upper magnetic current of 185 A, -5 C chuck temperature and 10.0 mtorr chamber pressure.

Two key results from the simulations are factors which determine the relative species fluxes to the wafer and which determine the radial plasma uniformity. The simulations indicated that the relative fluxes of various radicals to the substrate was strongly dependent on the ratio of electron dissociation cross-sections to wall recombination cross-sections. This suggests that modifications to the reactor walls such as heated or cooled liners could change the relative species fluxes. The simulations also indicated that the radial uniformity was a strong function of electrostatic potentials formed in the plasma which are affected by the electrical nature of the surfaces on which field lines terminate and on the spatial profile of the microwave power deposition.

Elements of simulation

Monte Carlo method

The simulation results which are presented here result from a Monte Carlo calculation of neutral and charged particle dynamics in a magnetized reactor. Neutral process gas particles are followed individually from their injection point at the gas manifold inlet located just below the microwave window until they reach the pumping port in the bottom of the chamber. During their residence in the chamber they suffer collisions with neutral and charged heavy particles; further, they may suffer electron impact collisions which lead to dissociation or ionization. In the case of ionization the charged ions are followed as they are pushed by the self-consistent electrostatic field towards the chamber walls where they neutralize and recycle. In the case of dissociation, the resulting fragments are followed individually until they react with the walls or are pumped from the system. As particles pass through computational volumes their velocities and dwell times within the volumes are recorded. By iterative accumulation of statistics of residence time within spatial cells, it is possible to arrive at a self consistent picture of the neutral and charged particle densities.

The Monte Carlo technique was chosen for this application because the mean free paths are comparable to the dimensions of the plasma and the system. It is thus difficult to compute the correct transport

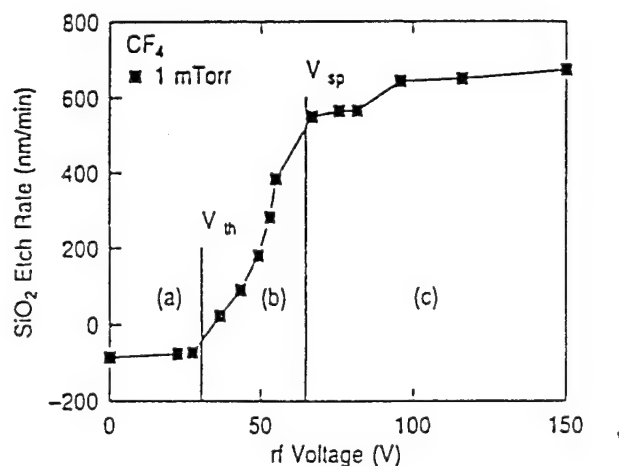


Figure (12) - Deposition and etching rates on silicon oxide as a function of RF voltage for a pure CF_4 feed gas. The microwave power was 1.0 kW and the neutral pressure 1.0 mtorr.

coefficients to be inserted in fluid equations. The Monte Carlo technique is also physically intuitive and allows the incremental inclusion of greater physical detail. The drawback is the computational time required for convergence because of statistical fluctuations resulting from finite numbers of particles and the difficulty of determining at what point the solution has converged to a steady state.

Determination of background distribution and bulk flows

Each Monte Carlo test particle collides with a background of neutral and charged heavy particles. This background distribution of particles, however, is precisely the solution to our problem and thus is not known *a priori*. We thus begin with a guess at the background distribution, launch a number of particles, accumulate statistics, correct the background distribution on the basis of the accumulated statistics and then repeat the cycle until the background distribution converges. We have found that in practice this procedure works well although we have not determined the optimal procedure for correcting the distribution function or the optimal ratio of launch particles to iterations.

Although the prescription outlined above appears straight forward, we have also found that in practice there are many subtleties. For example, in order to obtain the correct fluid limit it is necessary to account for effects of gradients in density and temperature. These are pressure gradients which drive bulk motions of the fluid which are balanced against viscous forces. In order to obtain this balance in a Monte Carlo simulation one needs to determine during a collision where the background particle last experienced a collision on the average and from which direction it is most likely that the background particle has come. As the mean free paths for particles become long compared to the scale size of the reactor, the viscosity effectively increases and gradients are spread out. In this limit such effects become weaker and this is the classical range of applicability for the Monte Carlo method. As the mean free path is decreased, however, a fluid limit is reached where pressure gradients lead to large bulk motions. In this limit, the iterative Monte Carlo approach described here becomes computational less attractive than a direct solution of the fluid equations.

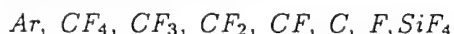
In the pressure regime of interest for the etching of SiN over GaAs , (2.0-10.0 mtorr) the mean free paths are comparable to sizes of the plasma while somewhat smaller than the size of the vacuum chamber which in our case is rather large. Thus the present case is a challenging simulation problem.

In the present case the bulk flows in the system are not driven by the gas input and pumping since the residence time of a non-reacting neutral is long compared to the reactor crossing time. Rather the bulk flows result from the ionization of neutrals which removes neutrals from the plasma region and rapidly transports them to a material surface such as the chuck or lower chamber walls where they neutralize. This creates an overall circulation where outside the plasma the flow is up and into the plasma where there is an effective sink.

Reactive chemistry

In addition to neutral argon which serves as a buffer gas for the system, CF_4 and O_2 are introduced into the system. These undergo electron dissociation as they enter the plasma. In the Monte Carlo simulation the subsequent dissociation products are tracked after the dissociation event and statistics accumulated in order to determine the spatial density profile and the flux to the wafer. Gas phase chemical interactions among radical species are ignored in the present simulation. These gas phase interactions can be calculated in an iterative fashion, although if the system is strongly dominated by gas phase chemistry, the Monte Carlo approach is probably not the optimal approach. We have found in practice that the probability of striking another radical before striking a material surface is small and that therefore, for this parameter range, the Monte Carlo approach remains accurate.

The species which are followed in the simulation are:



The oxygen containing species have been omitted from the simulation since their main effect is to eliminate the deposition of fluorocarbon films on the wafer and walls. Such deposition processes have also been omitted from the surface mechanism described below.

Only the SiF_4 etch product has been retained in order to study the effects of etch by-product loading on the system; other possible etch products of the SiN layer such as NF , N_2 , or SiF_n ($n = 0, 3$) have not been included. A estimate of the contribution of etch by-products to the total density can be obtained from typical etch rates for a 3.0 " wafer of 500 Angstroms per minute. This corresponds to a gas input of SiF_4 and nitrogen containing volatile by product of 0.24 sccm each, much less than the input gas flow of CF_4 of 11-33 sccm.

Gas throughput considerations

Although the above calculations indicate that the etching of the wafer should not heavily load the system or deplete the available atomic F , data indicate that the SiN_x etch rate increases with total gas flow. This indicates either a slow production or depletion of the rate limiting etch species within the reactor. However, the input gas flows of both O_2 and CF_4 are both larger than the effective input of etch by-products by the wafer and the relative species balance in the reactor is determined by the balance of dissociation and wall reformation which precedes on a time scale which is short compared to the residence time. This suggests that either the rate limiting reactant in the etch process is not atomic fluorine, but another species formed more slowly or that the atomic fluorine is being lost to the walls. No significant fluorocarbon film buildup can be seen by eye on the microwave window or anodized chamber interior; we therefore hypothesize that the wall loss could result from etching of the quartz microwave window or from reactions of atomic F with water trapped in the anodized aluminum walls to form HF which is then remains bound in the walls. There is some evidence that HF forms from the high mass 20 signal detected by an ion mass spectrometer attached to the chamber, although this signal could also arise from doubly ionized argon.

Radiation and metastables

In addition to dissociation, electron impact can also lead to optical excitations and the formation of metastables. These processes are included in the calculation of the total power deposited into the system only

through an effective power per ionization. This is equivalent to the assumption that photons and metastables are lost promptly to the walls. Although this is a good assumption for photons, argon metastables may play important roles through multi-step ionization and promotion of gas phase and surface processes which require an activation energy higher than the typical room temperature thermal energies.

Plasma Monte Carlo

As neutral atoms and molecules are tracked along their trajectories they suffer electron impact collisions which may lead to ionization. In the Monte Carlo approach, these charged ions are also followed and their statistics accumulated giving an approximation to the ion density and velocities. Because the ions are charged they experience forces due to the static magnetic field which is imposed on the system and due to the electrostatic potential.

Magnetic field calculation -

The static magnetic field is calculated using a finite element code MAP written by Robert Pillsbury, Jr.. The present code is based on the grid structure derived from the finite element representation. The code contains the possibility for computing the effects of iron although this capability was not used in the present simulation.

Electrostatic potential calculation

The transport of ions is determined by the balance between the drive outward due to the spatial profile of the electrostatic potential and the drag due to ion-neutral collisions and by diffusion due to ion-neutral collisions. On the other hand the potential results from the differing transport of ions and electrons both along and across magnetic fields. Thus an understanding of the fundamental processes affecting radial uniformity of ion fluxes requires an understanding of the electrostatic potentials.

The electrostatic potential arises in order to equilibrate electron and ion densities. Because of the relatively high plasma densities ($1 \times 10^{11} - 1 \times 10^{12} \text{ cm}^{-3}$) within the plasma very small charge imbalances lead to large electric fields. The plasma is thus quasi-neutral ($n_i^+ = n_e$) and the potential is determined by the momentum balance of electrons along a field line. The leading terms in the electron momentum balance equation in steady state are:

$$0 = en_e \nabla \phi - \nabla n_e T_e.$$

The solution to this equation for constant electron temperature, is an exponential dependence of electron density on potential,

$$n_e \propto e^{e\phi/T_e}$$

Potential sheaths form at the walls where quasi-neutrality breaks down and these serve to equilibrate the electron creation and loss rates as required for steady state. Since positive ions are created at the same rate as electrons, the sheaths can also be viewed as retarding electron losses in order to maintain a net quasi-neutral plasma. In this simulation we do not take into account the effects of negative ions. In the low pressure, high plasma density regime treated here, the detachment rate for negative ions exceeds the attachment rate and the plasma is in general electropositive.

The bulk electron distribution in ECR systems has been measured by Langmuir probe and laser induced fluorescence to be a Maxwellian with typical temperatures in the 2-6 eV range although theoretically a heated tail is expected. For the simulation results here we make the further simplifying assumption that the electron temperature is a constant along a field line giving for the electron energy distribution function:

$$f_e = f_e^0 \exp(-\epsilon/T_e) = f_e^0(\psi) \exp(-(1/2mv^2 - e\phi)/k_B T_e(\psi))$$

where k_B is Boltzmann's constant, ϕ is the electrostatic potential and ψ is the magnetic flux which is constant along a field line. This form of the distribution function is exact when the electron mean free path along the field line is long compared to the size of the chamber and when the electron density is sufficiently high that

electron-electron collisions relax the distribution towards a Maxwellian more quickly than the microwave fields and inelastic collisions are able to distort the distribution away from a Maxwellian.

The first moment of the the electron distribution function above gives an exponential relation between the electron density, n_e , and the electrostatic potential, ϕ along a field line:

$$n_e = n_e^{\min}(\psi) e^{(e(\phi - \phi_0(\psi))/T_e(\psi))}$$

where $\phi_0(\psi)$ is a constant and corresponds to the potential at the point along the field line where the density is a minimum and equal to $n_e^{\min}(\psi)$. This exponential form satisfies the electron momentum balance equation to leading order as discussed above. Given an ion density which by quasi-neutrality equals the electron density this exponential relation between density and potential determines the variation of the potential along the field line up to a constant, $\phi_0(\psi)$ which can vary from field line to field line.

The potential variation across field lines is not governed by electron momentum balance since the electrons are tightly bound to each field line, but by the variation of ϕ_0 and T_e as a function of magnetic flux. The electron temperature on a field line reflects the balance between the microwave electric fields which heat the the electrons and inelastic collisions which cool the electrons. Thus the variation of T_e across field lines is determined by the microwave field pattern and the radial thermal conduction of electron due to electron-electron scattering. Because we do not solve for the microwave fields or the electron radial power flow, we impose an analytic variation of T_e on magnetic flux which we discuss below.

The quantity ϕ_0 is determined by equating the electron creation rate on a field line to the loss rate out the ends of the field line to material objects. The height of the sheath and hence the loss rate from the flux tube depends on the depends on the overall additive constant ϕ_0 and the potential of the material surface itself. In the case of metallic walls which are grounded this potential is zero and ϕ_0 depends only on the creation rate inside the flux tube. We can write this balance between creation an losses as follows:

$$\sum_{\text{ends}} \frac{v_{\text{th}}^e}{4} \frac{1}{B_{\text{wall}}} n_e^{\min} e^{-e\phi_0/T_e} = \int \frac{dl}{B} n_e n_0 < \sigma_{\text{ion}} v > .$$

Given an electron density as determined from the ion density, this determines ϕ_0 . Note that on field lines where the electron temperature, and therefore the creation rate, are high, the sheath potential drop *relative to the electron temperature* is smaller than on field lines for which the ionization rate is low. However, the *absolute* sheath potential drop is higher as we now show for the case of a Maxwellian electron distribution.

As we discuss below the assumption of a Maxwellian electron temperature implies that the leading order dependence of the ionization rate is exponentially dependent on the inverse of the temperature. Rewriting the expression above for ψ_0 by taking the natural logarythm of both sides gives:

$$e\phi_0 = -T_e \ln \left[\frac{4B_{\text{wall}}}{v_{\text{th}}^e n_e^{\min}} \int \frac{dl}{B} n_e n_0 < \sigma_{\text{ion}} v >_0 \right] + \epsilon_{\text{thres}}$$

where ϵ_{ion} is the threshold energy for ionization. The quantity in curly brackets is always less than one and thus the overall additive constant to the potential, ϕ_0 , varies to lowest order with electron temperature. This is, in fact, a key insight into determining the electrostatic potential structure and hence the radial transport of ions.

We have discussed thus far the case for a metallic boundary. For an insulating boundary the electron loss rate is determined by the difference between the overall potential of the field line and the potential of the surface, ϕ_{surface} . This latter quantity must be determined in order to equilibrate ion and electron fluxes locally to the insulating surface. Thus for example, if the microwave window initially experiences more electron than ion flux, it will charge negative in order to repel electrons and attract ions.

Summarizing the disscusion thus far, given an ion density as function of space, and ion fluxes to insulating surfaces we can determine the potential structure. However, the ion density itself depends on the

electrostatic potential. We have developed an iterative algorithm by which the electrostatic potential is corrected successively in order to achieve self-consistency. As part of this program we also developed a numerical scheme based on a psuedo-time stepping method to improve this convergence, however, this was not implemented for the results shown below.

Electron rates

The electron rates for excitation, dissociation and ionization depend on the form of the electron distribution function. Typically these processes involve the higher energy portion of the electron distribution. In the results presented here the electron distribution function is approximated by a Maxwellian leading to an exponential dependence of the rate on the electron temperature. We approximate the cross sections for all processes to be linearly rising in energy above a threshold energy:

$$\sigma = \begin{cases} 0 & \text{if } \epsilon < \epsilon_{\text{thres}}; \\ \frac{\sigma_0}{\epsilon_s}(\epsilon - \epsilon_{\text{thres}}) & \text{if } \epsilon > \epsilon_{\text{thres}}; \end{cases}$$

Each process is characterized by a threshold energy, the derivative of the cross-section with respect to energy which is expressed as a value for the cross-section, σ_0 , together with the incremental energy above threshold corresponding to that value, ϵ_s . We show in Table (3.) the values of threshold energy, ϵ_{thres} , cross-section, σ_0 , and ϵ_s , for ionization and dissociation processes. The electron rate as a function of electron temperature given these parameters for a Maxwellian electron distribution with temperature T_e is:

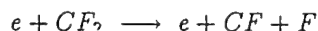
$$\langle \sigma v \rangle = \frac{2}{\sqrt{\pi}} \sqrt{\frac{2T_e}{m_e}} \frac{\sigma_0}{\epsilon_s} \epsilon_s e^{-\epsilon_{\text{thres}}/T_e}$$

Also shown in Table (3.) are calculated values for $\langle \sigma v \rangle$ for a typical electron temperature.

In determining the electron density the electron temperature along the field line was taken to be constant. However, the higher energy portion of the electron distribution which is important for ionization and dissociation processes experiences more inelastic collisions than the lower energy portion and therefore the number of high energy electrons will decay as one moves away from the resonance zone; this effectively reduces the electron temperature in the high temperature tail. We model this by multiplying the rate by a form factor which decays away from the resonance zone.

Surface Processes

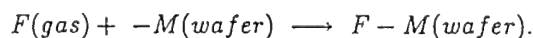
In a neutral pressure regime of the experiments, gas phase particles and atoms are in good contact with the walls. We found that the density of radicals such as CF_2 depended on the interplay between electron dissociation which destroys via the reaction:



with a rate proportional locally to $n_e \langle \sigma_{\text{dis}} v \rangle$, and the wall reaction probability in which CF removes an adsorbed F ; (denoted as $F - M$), from a material surface and returns to the gas phase as CF_2 :



Gas phase species are also allowed to adsorb onto free surface sites denoted as $-M$. For example, atomic fluorine adsorbing onto the wafer is denoted as:

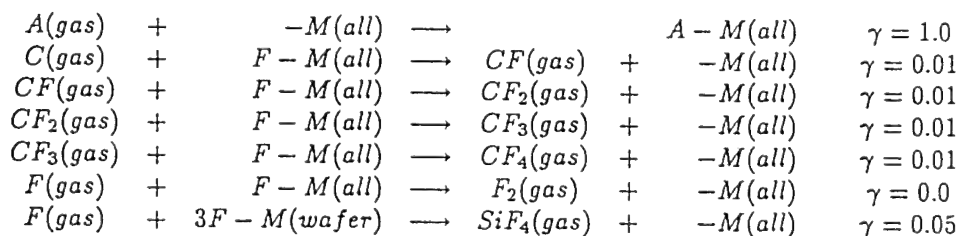


A reaction probability is assigned to each such reaction which we denote by γ . Note that the areal density of free surface sites, $-M$, is followed in the simulations.

T _e =	2							
ionization								
species	e thres	sigma	e scale	sigma 0	v	sigma 0*v	sigma 0*v*exp(-e _i /T)	
Ar	15.76	7.87E-17	5.24	3.3488E-16	8.60E+07	2.88E-08	1.0893E-11	
cf4	16.5	4.70E-17	5.4	2.0134E-16	8.60E+07	1.7315E-08	4.5236E-12	
cf3	8.9	4.70E-17	5.4	1.2669E-16	8.60E+07	1.0896E-08	1.2725E-10	
cf2	11.42	4.70E-17	5.4	1.5144E-16	8.60E+07	1.3024E-08	4.3145E-11	
cf	9.1	4.70E-17	5.4	1.2866E-16	8.60E+07	1.1065E-08	1.1692E-10	
c	11.2	4.70E-17	5.4	1.4928E-16	8.60E+07	1.2838E-08	4.7474E-11	
f	17.4	4.70E-17	5.4	2.1017E-16	8.60E+07	1.8075E-08	3.011E-12	
SiF4	15.7	4.70E-17	5.4	1.9348E-16	8.60E+07	1.6639E-08	6.4851E-12	
dissociation								
species	e thres	sigma	e scale	sigma 0	v	sigma 0*v	sigma 0*v*exp(-e _i /T)	
cf4	13	4.27E-17	3.7	2.2138E-16	8.60E+07	1.9039E-08	2.8623E-11	
cf3	13	4.27E-17	3.7	2.2138E-16	8.60E+07	1.9039E-08	2.8623E-11	
cf2	13	4.27E-17	3.7	2.2138E-16	8.60E+07	1.9039E-08	2.8623E-11	
cf	13	4.27E-17	3.7	2.2138E-16	8.60E+07	1.9039E-08	2.8623E-11	
SiF4	13	4.27E-17	3.7	2.2138E-16	8.60E+07	1.9039E-08	2.8623E-11	

Table (3.) - Table showing parameters used in calculating electron ionization and dissociation rates as a function of electron temperature. Rates as calculated using a Maxwellian are given for a typical electron temperature as an example.

We list below the thermal neutral reactions implemented in the simulations:



The last reaction is isotropic chemical etching of the SiN wafer layer to produce gas phase SiF₄. Note that the fluorocarbon deposition processes and their removal by atomic oxygen have not been included in the simulations.

Since the reaction probabilities for these various processes have not been measured, the values of γ have been estimated in order to reproduce data from another ECR reactors in which the relative concentrations of ions entering a pinhole in the substrate were measured.¹³ These experiments were performed on an ECR reactor in which the source chamber consisted of a 6.0 cm radius cylinder with an anodized aluminum liner mounted on a larger wafer chamber at a microwave power of 1000 W, a pressure of 1.0 mtorr for a pure CF_4 feed gas. The relative ratios of ions detected is listed below:

$$\begin{array}{rcl} \frac{C^+}{F^+} & & 2.5 \\ \frac{C^+}{CF^+} & & 5.0 \\ \frac{C^+}{CF_3^+} & > & 10.0 \\ \frac{C^+}{CF_2^+} & > & 20.0 \end{array}$$

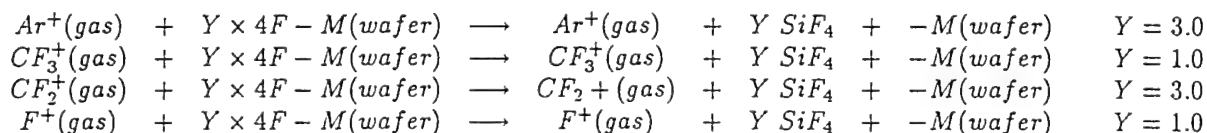
Since CF_4 dissociatively ionizes to form CF_3^+ , the high ratio of C^+ to CF_3^+ indicates that the original CF_4 has been highly dissociated. These numbers indicate that the reformation of more highly fluorinated species on the walls is a slow process.

On the other hand an experiment was performed in which an ion mass spectrometer was attached to the chamber through a metallic bellows tube connected to the main chamber through an access port at the level of the wafer. The mass spectrometer ionizer was on to sample neutrals. The results showed a high signal at a mass corresponding to CF_3^+ which is the main cracking product of CF_4 . Other dominate signals were identified as Ar , Ar^{++} or HF^+ , $C_2H_3^+$ or HCN^+ , CF_2^+ . These results, which must be treated very carefully due to uncertainties in the cracking patterns and recombination within the mass spectrometer.

We note that the reactor size will play a role in the relative dissociation of the feed stock gas. The reactor of Oehrlein *et al.* is smaller than the present reactor. If we taken the volumetrically integrated dissociation rate to be simply a function of total microwave power, then the losses will scale as the surface areas assuming the reaction probabilities on each surface are similar.

The numbers which are listed above for the reaction probabilities used in the simulations give a relatively high dissociation fraction, but the depletion of atomic F on the walls has not been included.

A model of ion enhanced reactive sputtering was also implemented in terms of the yield, Y , per ion of sputtered material. The reactions implemented were:



The yields were adjusted in order to give the observed etch rates.

In summary, a detailed surface model was therefore implemented which takes into account adsorption of species on the walls, surface reactions leading to removal of previously adsorbed species, ion enhanced removal of species from the wall. The adsorbed surface concentration of the various species is allowed to evolve self-consistently. Although many of the reaction rates are not known *a priori* the fitting of these rates to the data helps in identifying the main surface chemistry processes.

Microwave fields

The effect of the microwave field is to determine the temperature of the electron distribution function. In the simulations shown, the microwave fields were not solved self-consistently and therefore we model the effects of the field structure by the choice of the electron temperature profile. Many of the experimental ion saturation current traces indicate a relatively flat or hollow radial profile. This would be consistent

with the microwave field pattern of a predominantly surface wave which propagates along the outside of the plasma column. We model this by using a Lorentzian functional form where the electron temperature has a maximum T_e^{\max} , at specified heating flux ψ_{heat} , with different decay lengths inside and outside the peak heating surface. The inner drop off length determined by specifying the electron temperature on axis, T_e^{axis} , and the outer drop off length is determined by choosing the flux point where T_e drops by one half:

$$T_e(\psi) = \frac{a}{a + (1 - x)^2}$$

$$x \equiv \frac{\psi}{\psi_{\text{heat}}}$$

$$a = \begin{cases} \frac{R_T}{1 - R_T} & \text{if } x < 1 \\ (1 - x_{1/2})^2 & \text{if } x > 1 \end{cases}$$

$$R_T = \frac{T_{\text{axis}}}{T_{\max}}$$

The value of ψ_{heat} is chosen to correspond to the flux tube which maps to the edge of the microwave window. For the simulations shown the values of the parameters were as follows:

$$\begin{array}{ll} T_e^{\max} & 3.6 \text{ eV} \\ T_e^{\text{axis}} & 2.9 \text{ eV} \\ x_{1/2} & 2.0 \end{array}$$

Simulation results, comparison to experiment and interpretation of data

Plasma profiles

Improvements in the radial ion flux uniformity allow a reduction in the overetch time required to clear the *SiN* overlayer. During this overetch step, portions of the *GaAs* substrate are necessarily exposed to the plasma. Since we hypothesize that damage is introduced during early during the plasma exposure, a significant win is to be had in reducing time. In addition, the use of this reactor system in other contexts will require using larger wafers. It is therefore of great value to understand the key elements which determine the ion radial profiles. We have studied in great detail the effects of potential profile on ion density and transport and discuss these below.

For the remainder of this report we will focus on the results of a representative simulation. Unless otherwise noted, the parameters for the simulation results shown are as follows:

Microwave power	1.0 kW
Neutral pressure	2.3 mtorr
Ar flow rate	12.5 sccm
CF4 flow rate	11.0 sccm

We show in Figure (13) a trace of ion saturation current versus radius for a variety of different microwave powers. Note that the profile is mildly to strongly hollow, with generally an increasing hollowness in ion saturation current. There is also evidence of mode jump or transition from one equilibrium state to another as the power is increased from 600 W to 700 W. Such jumps are common in ECR sources and result from the non-linear coupling between the microwave fields and the plasma. The reasons for the hollowness we hypothesize are:

- The peaking of the microwave power deposition and hence the ionization function on the surface of the flux tube which maps to the microwave window.
- The interplay between the magnetic confinement of electrons and the mobility and diffusive driven transport of ions which creates cross-field potential structures which inhibit ions towards the axis.

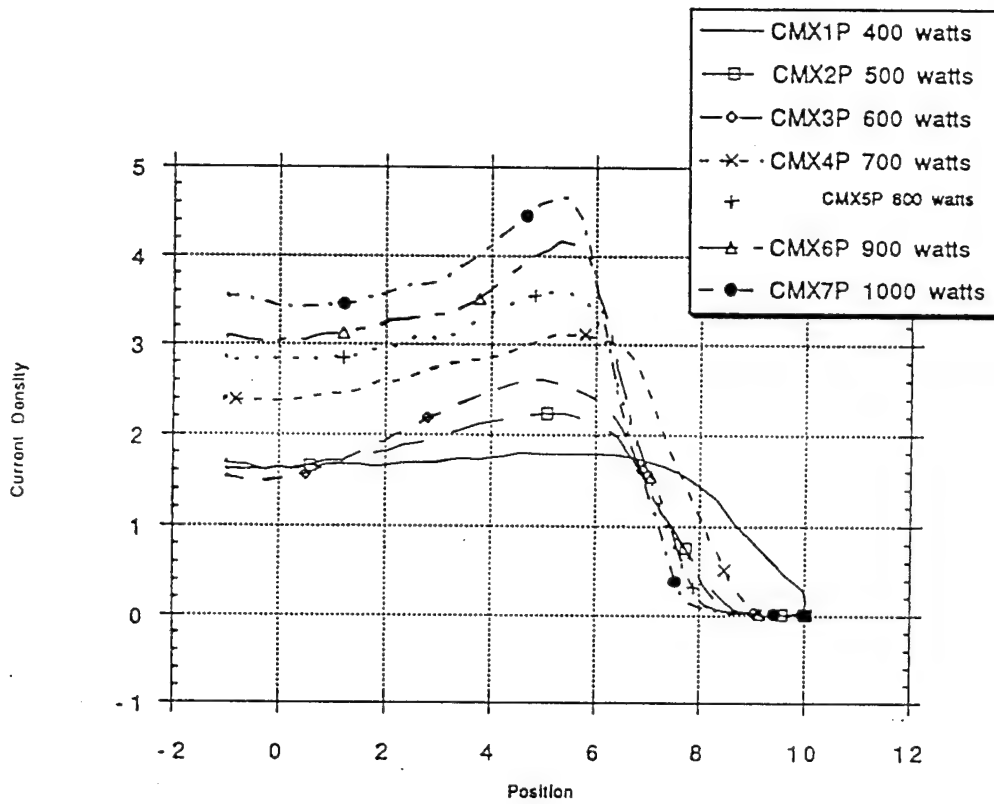


Figure (13) - Ion saturation current as a function of radius

We show in Figures (14) and (15) contours of constant electron density and electrostatic potential from the simulations. With these as with the remaining figures showing simulation data, there is a certain amount of statistical noise due to the Monte Carlo method. This is particularly true near the axis where the relative phase space volume is small. The reader thus must look for the general trends and ignore the fine scale structures.

Axial ion transport

Ions are born primarily near the resonance zone located a few centimeters below the upper chamber cover. They are then accelerated downward axially and outward radially by electrostatic fields. In the downstream region away from the ionization source the ion transport is given approximately in steady state by:

$$0 = -\frac{\partial}{\partial z} (m_i n_i v_i v_i) - \frac{\partial}{\partial z} (n_i T_i) - e n_i \frac{\partial \phi}{\partial z} - n_i v_i m_i \nu_i$$

where z is the coordinate in the axial direction and only axial components of the velocity are indicated. If the flow is sub-sonic and the ion temperature is much less than the electron temperature (which is a good approximation), then remaining terms indicate that the flow is driven by the potential away from the ionization source region and is retarded by ion-neutral collisions. Since the potential and electron densities are related by an exponential relation, the gradient in the electrostatic potential is reflected in the gradient of the electron density which decays away from the resonance zone. If we substitute this exponential relation into the ion momentum balance equation above and approximate the ion flux density, $n_i v_i$, as decaying geometrically as $1/z^2$, then we obtain a $\frac{1}{z}$ axial decay of electron density in the region away from the resonance zone:

$$0 = -e n_i \frac{\partial \phi}{\partial z} - n_i v_i m_i \nu_i = -\frac{\partial}{\partial z} (n_i T_e) - m_i (n_i v_i)_0 \left(\frac{L_{fall}}{z} \right)^2 \nu_i$$

$$n_i \propto \frac{1}{z}$$

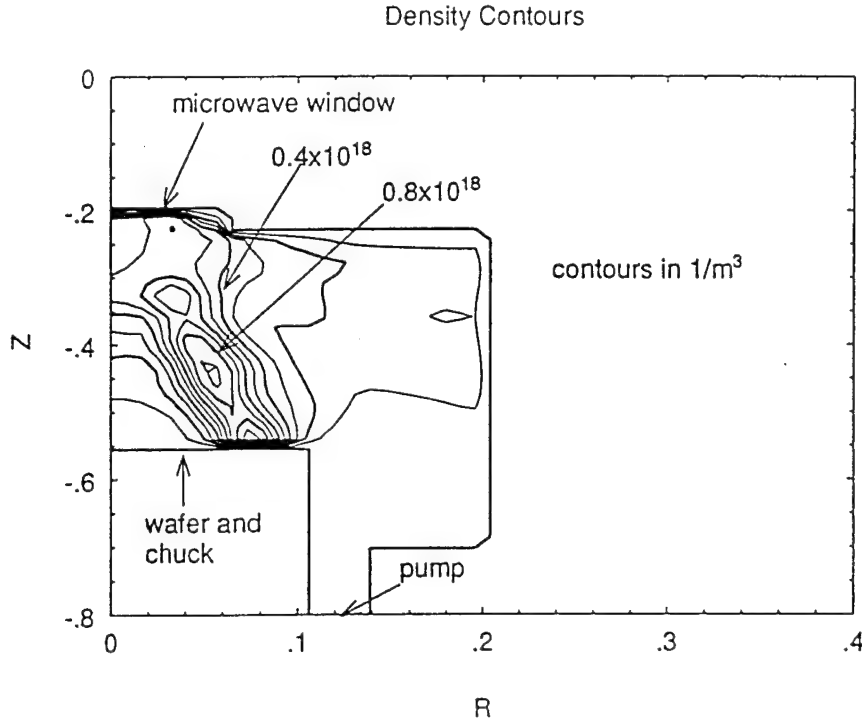


Figure (14) contours of constant electron density from the simulation. Note that the fine structure is due to statistical fluctuations due to finite simulation test particles and is not real.

resonance zone:

$$0 = -en_i \frac{\partial}{\partial z} \phi - n_i v_i m_i \nu_i = -\frac{\partial}{\partial z} (n_i T_e) - m_i (n_i v_i)_0 \left(\frac{L_{fall}}{z} \right)^2 \nu_i$$

$$n_i \propto \frac{1}{z}.$$

Cross-field ion transport

The cross field ion transport is determined by the interplay between the magnetized electron transport processes and the diffusion-mobility driven ion transport processes and the fact that the central flux tubes terminate at one end on a dielectric window and on the other end on an electrically floating chuck. We find in the simulations that if the chuck is grounded that there is a net ion current to it. This is due to the peaking of the ionization function on the flux tube which maps to the edge of the dielectric window. This flux tube surface passes outside of the chuck edge; therefore electrons generated on this surface strike the grounded lower chamber wall and not the chuck. However, the corresponding ions which are born at this flux tube surface are able to diffuse inward and strike the chuck charging it positive. If the chuck is floated, it will charge sufficiently positive to repel inwardly diffusing ions. This leads to a mildly hollow profile as seen in the experiment and in the simulations when these effects are included. We note that radial potential variations due to surface or chuck charging which are on the order of the electron temperature have a strong effect on the ion radial transport and can change the profile from a hollow profile to a peaked axial profile.

Relation between cross field potential, electron temperature and electron density profiles.

We summarize at this point some of the qualitative relations between the cross field variations of potential, density and temperature. We consider several cases:

- *Peaked potential, peaked density, peaked electron temperature.* Recalling the discussion above, the absolute sheath height will in general scale with electron temperature. Thus if all flux tubes terminate on

Potential Contours

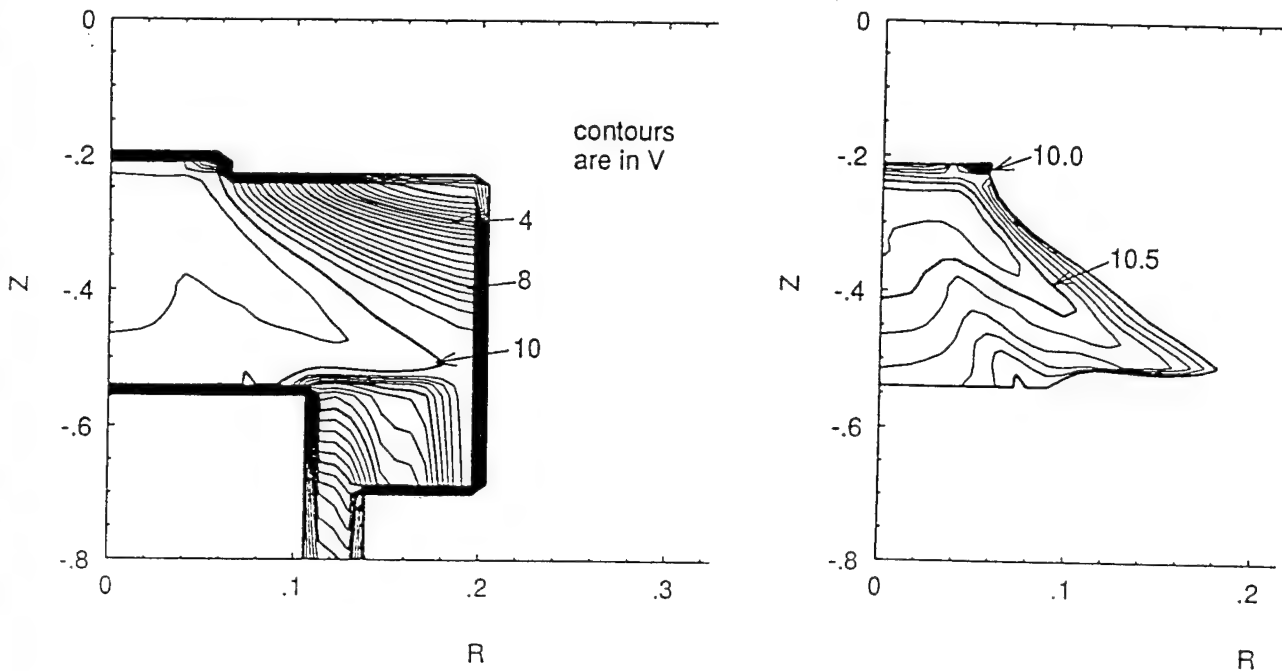


Figure (15) contours of constant electrostatic potential from the simulation corresponding to the electron density profile shown in Figure (14). The wafer in the simulation floats at a potential of 3.0 V above ground and the outer stainless steel hold down ring at 1.5 V 3.0 V above ground. The Figure on the left shows all the contour lines and the Figure on the right shows the contour lines in the flat plasma region.

grounded surfaces a radially peaked electron temperature will in general produce a peaked potential. Since the ionization function will follow the electron temperature except if there is a strong neutral depletion in the plasma and since the potential accelerates ions radially, the resulting electron density profile will also be peaked on axis.

- *Hollow electron temperature, hollow potential, peaked density.* If the electron temperature is hollow and the flux tubes terminate on grounded surfaces, the potential will be hollow which will tend to collect ions towards the center. Depending on the nature of the depth of the potential this can lead to a narrow concentration of ions on axis together with an outer more diffuse skirt of ions. It is difficult to construct a picture by which such a hollow potential could produce a hollow density profile
- *Hollow electron temperature, peaked or multiple maxima potential, hollow density profile, insulating surfaces.* If flux tubes terminate on insulating surfaces the absolute sheath drop may increase radially, but the positive charging of the insulator surfaces on axis may lead to a potential profile peaked on axis. There may be an additional maxima at the point of heating. Such a multiple maxima potential profile will produce the characteristic hollow density profiles measured in this experiment. Note that the electron temperature may itself have a maxima on axis, decrease with radius and then increase to another maxima due to the presence of a surface mode and a bulk mode; such a profile could also lead to a hollow density profile

Supporting evidence for model

The model proposed to explain the ion density profiles involves strongly magnetized electrons, mobility driven ions and surface charging. Supporting evidence for this model can be found in the traces found on the walls of the inside of the upper anodized aluminum vacuum chamber. This chamber has vertical rows of

permanent magnets. Clear patterns which resulted from these magnets could be seen on the side walls of the chamber and on the top stainless steel vacuum chamber cover on which the microwave window is mounted. These traces are presumably from either deposition differences due to the presence of ion fluxes or changes in the anodization due to ion bombardment. These patterns have spatial features on the order of 1.0-3.0 mm which is considerably smaller than the ion Larmor radius in the combined axial and permanent magnet fields. The patterns can be explained in terms of electron flows which are highly magnetized coupled, the electrical properties of the materials on which the field lines terminate (dielectric window, anodized aluminum or stainless steel) and the requirements of quasi-neutrality and equal ion and electron fluxes to insulating surfaces. The fine spatial scales of the features also suggests that rapid electron cross-field transport is not present. This is an extremely important observation, since rapid electron radial particle transport would undermine a basic hypothesis of the model.

A test of this model would be to explore the changes in the ion saturation current profile as a function of changing the electrical properties of the chuck. We propose to undertake such tests during Phase II.

Total Neutral Density

The total neutral gas density is shown in Figure (16) for the low pressure configuration. Note that the total density is extremely flat with only a slight depression in the plasma region and a slight increase immediately below the microwave window. This is due to the ionization of the plasma neutrals as they enter the plasma regions. Since the ion velocity is large compared to the neutral velocity, argon neutrals which are ionized move quickly to the walls where they recombine. This effect can be much larger when either the plasma is more localized, more intense or more constricted by closely fitting walls and can lead to pressure differentials of a factor of two. In this case the effect is relatively slight.

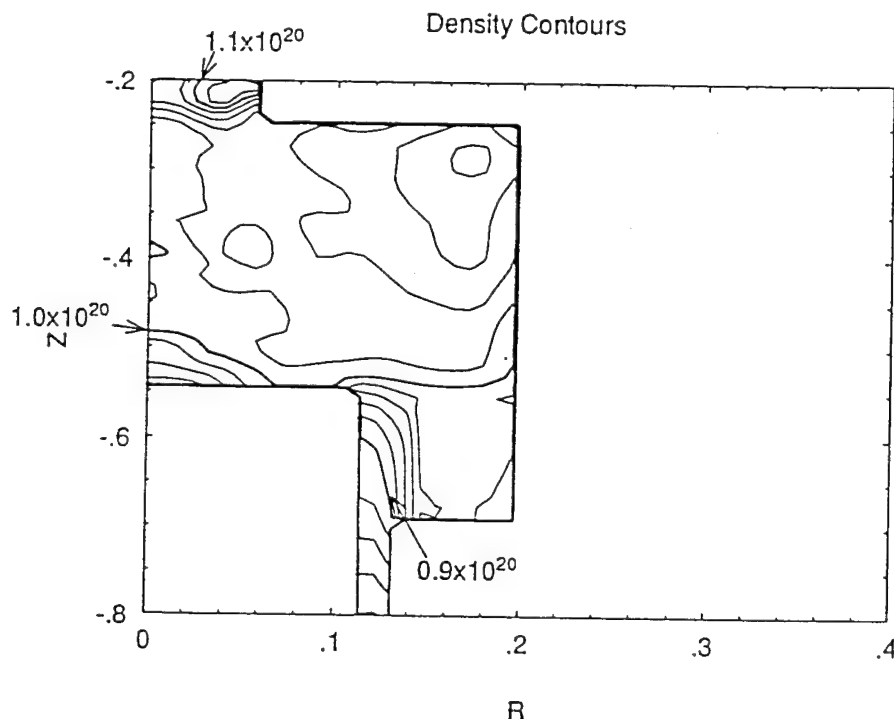


Figure (16) contours of constant total neutral density

The bulk flow patterns from the simulation are shown in Figures (17) and (18) which show contours of constant axial and radial flows. Note first that in this low pressure regime that the flows are relatively small compared to the thermal velocities of $\approx 3.0 \times 10^2$ m/sec and therefore are very noisy due to statistics in the

Monte Carlo simulation. This is not the case at higher pressures above 10.0 mtorr where these flows become considerable. The flows result from the pumping action of the plasma which removes neutral particles from the resonance zone region and deposits them on material surfaces at the ends of the corresponding flux tubes. This leads to bulk neutral flows into the plasma and away from surfaces which appear as a sink and sources respectively.

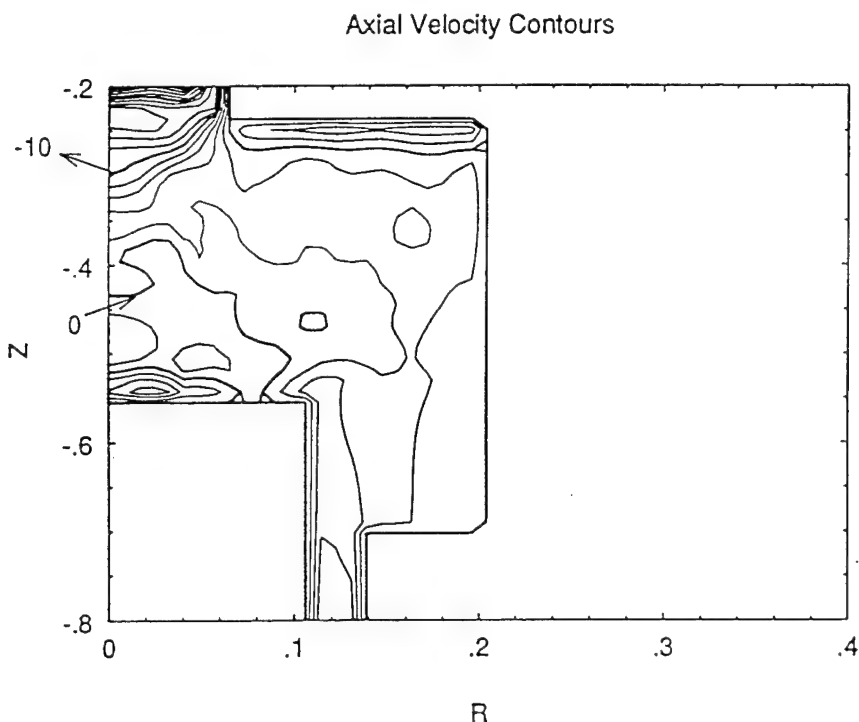


Figure (17) contours of constant axial flow.

Reactive species

We show in Figure (19), (20), (21), (22), (23), (24), (25), (26) contours of constant density for the species Ar , CF_4 , CF_3 , CF_2 , CF , C , F and SiF_4 respectively. These are in general rather featureless except for an increase in density near the gas inlet port located at the microwave window and a decrease in the passage to the pump port. This indicates that the dissociation and wall recombination processes are slow compared to the typical transit time between the plasma and the walls. This is to be contrasted to cases in which both dissociation and wall losses are rapid in which large gradients develop in species concentrations. The relative species concentrations reflect the interplay between the dissociation rates and the wall reaction probabilities chosen for each species. We note that in higher power and larger radius plasma systems that such species gradients are common.

The average particle residence time in the device is 0.33 seconds which is very long compared to the typical neutral reactor crossing time of 1.0 msec. Thus the simulations predict that to lowest order the relative equilibrium between species is largely independent of reactor throughput. In the simulations film deposition on the reactor walls has been set to zero and possible formation of HF has not been included.

Proposed Redesign of Reactor

The goal of this project is the redesign of the ECR reactor and development of a process to reduce the damage to $GaAs$ during etching of SiN overlayers. The results of the Phase I indicate that ion bombardment energy is not the key factor initially envisioned, rather ion current density appears to play the major role.

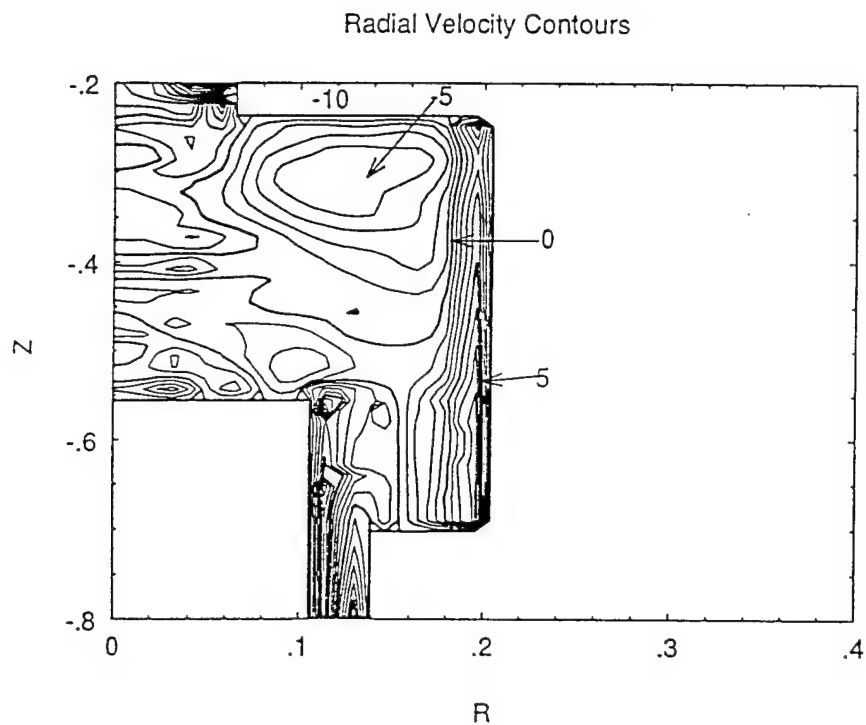


Figure (18) contours of constant radial flow.

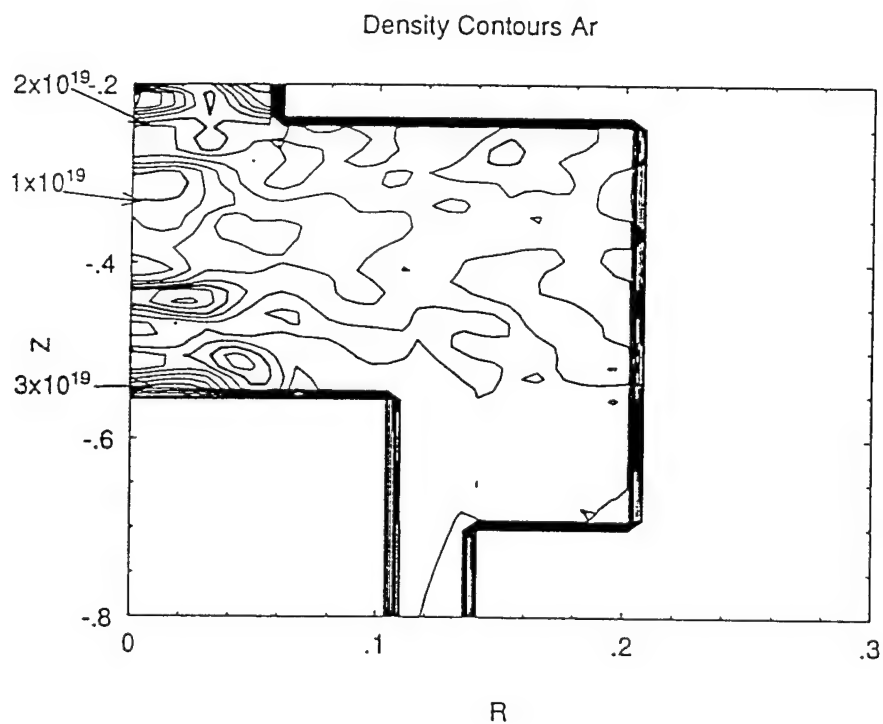


Figure (19) contours of constant Ar concentration.

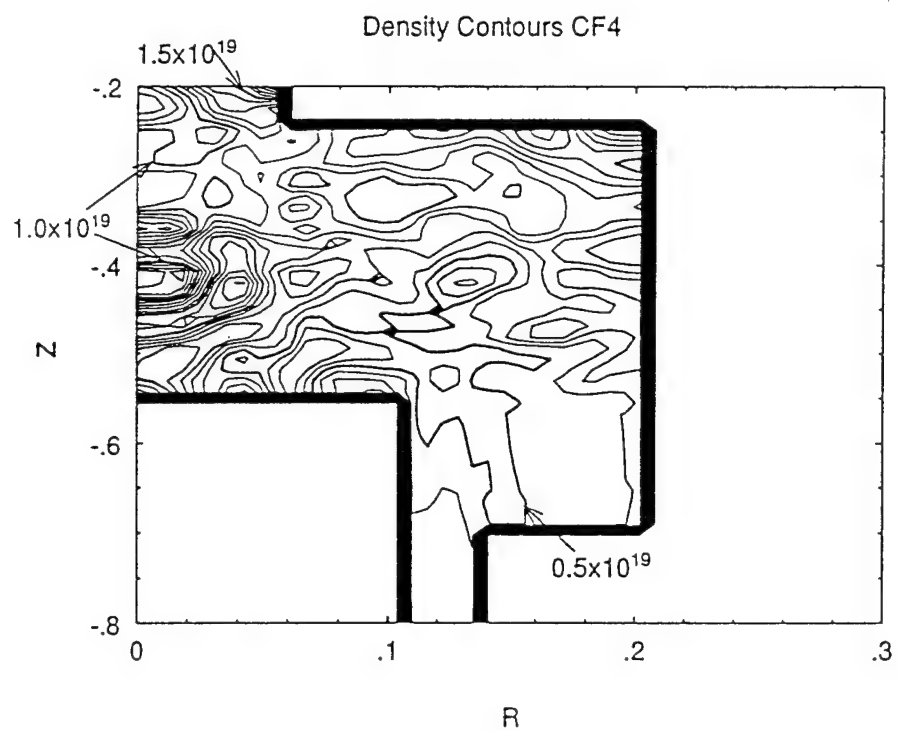


Figure (20) contours of constant CF4 concentration.

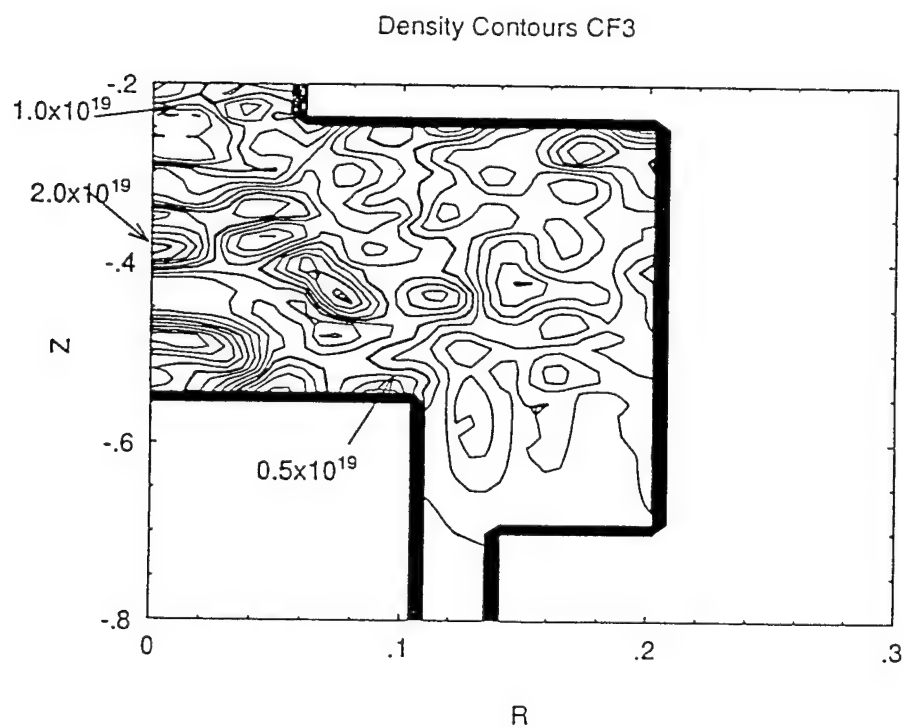


Figure (21) contours of constant CF3 concentration.

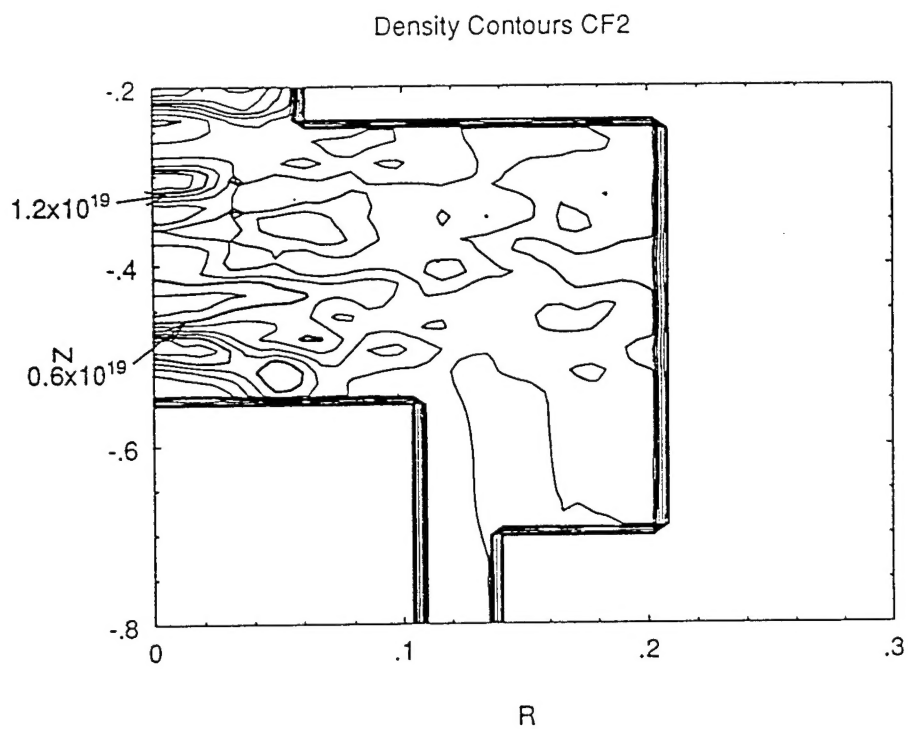


Figure (22) contours of constant CF2 concentration.

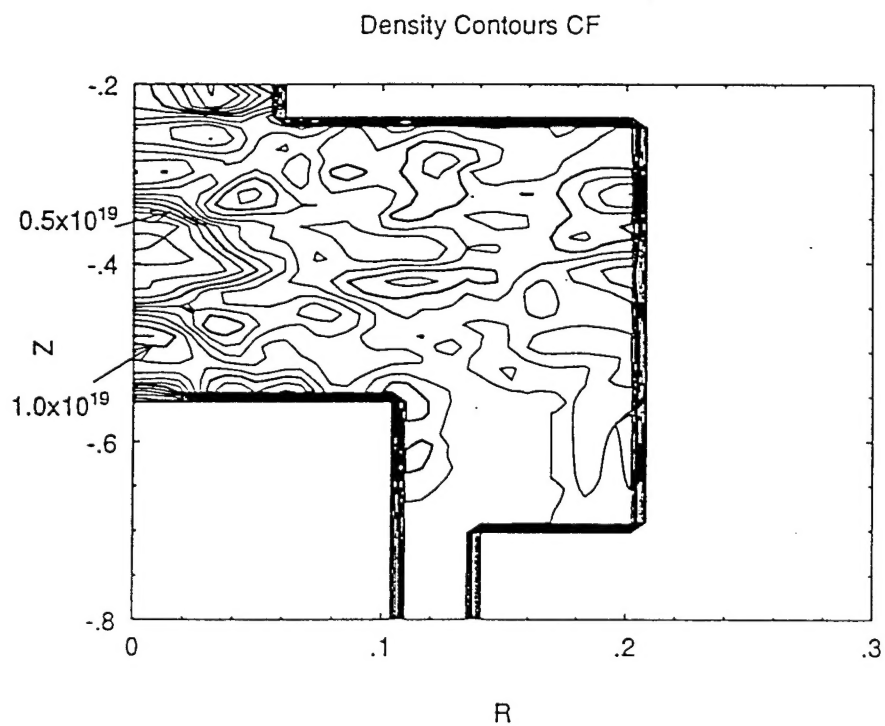


Figure (23) contours of constant CF concentration.

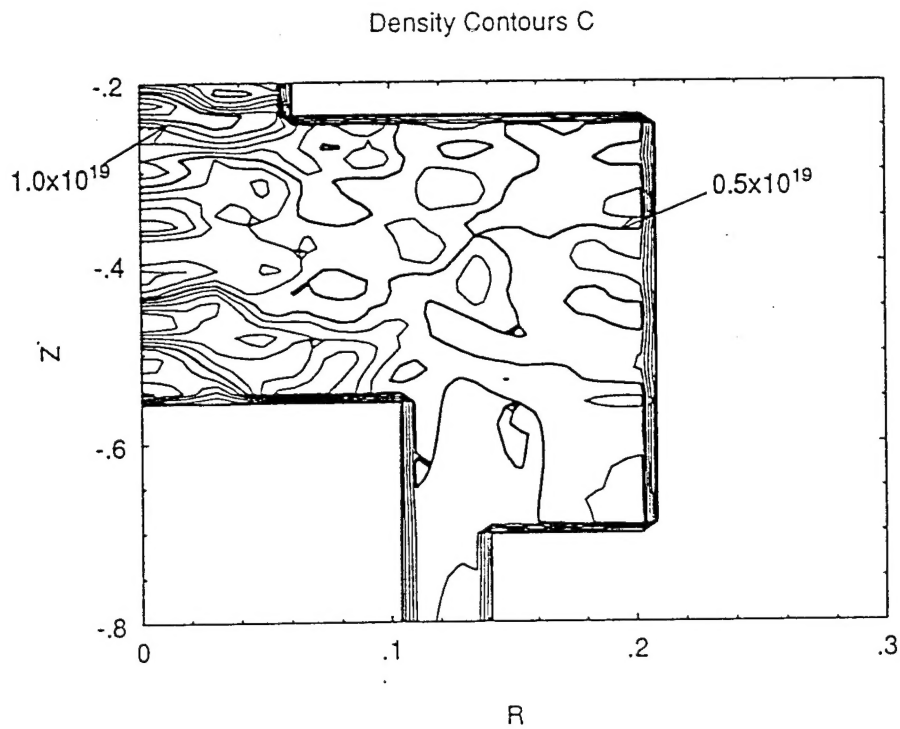


Figure (24) contours of constant C concentration.

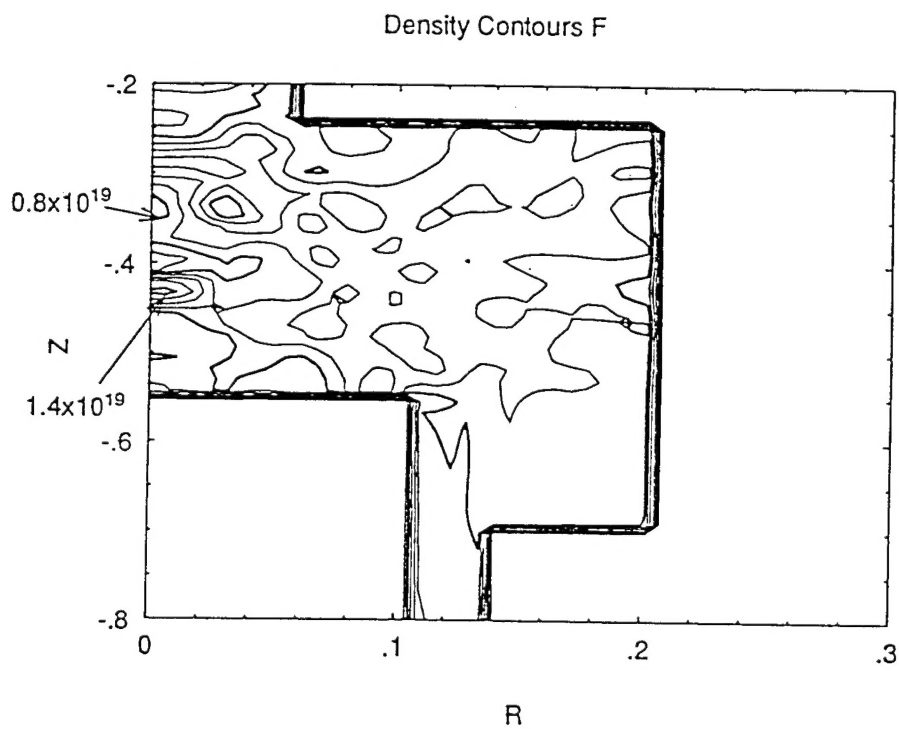


Figure (25) contours of constant F concentration.

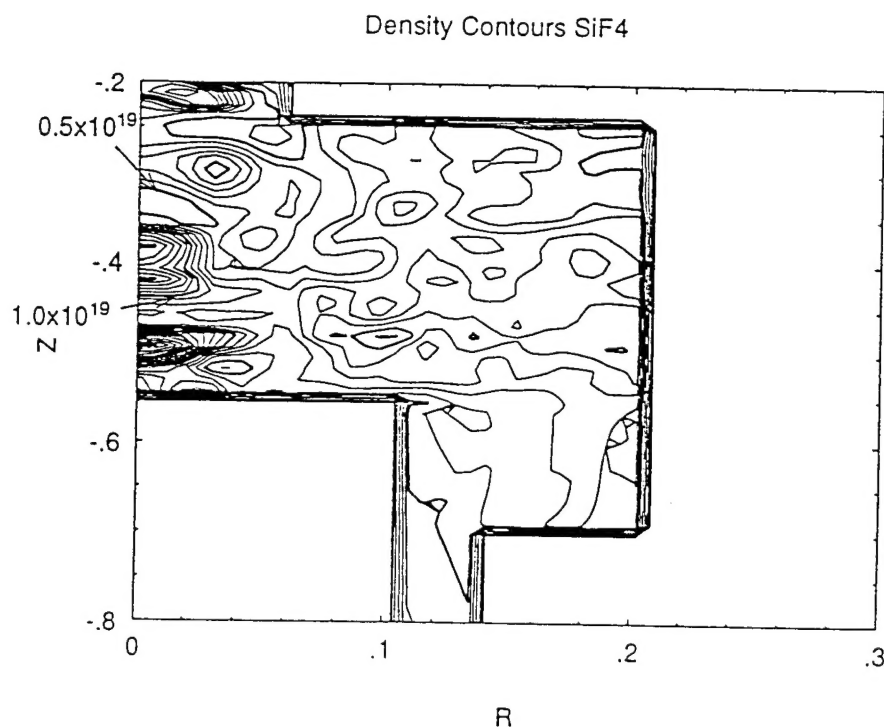


Figure (26) contours of constant SiF₄ concentration.

There are also indications that the ion damage occurs during the initial exposure of the *GaAs* crystal substrate to the plasma. This occurs as the *SiN* overlayer is cleared. Because the clearing process has a radial dependence, an overetch time is required in order to remove the *SiN* from the entire wafer. It is during the overetch that the damage occurs. This suggests that employing a multi-step process with active control via real time diagnostics. We envision the following set of modifications to the reactor system:

1. The development of a sensitive set of end point diagnostics with spatial resolution over the wafer in order to be able to actively change processes as the *SiN* clears.
2. The optimization of radial uniformity in order to minimize the overetch time required. The possibility of using a novel microwave launch structure which has been developed by ASTeX for other applications will be evaluated in this context.
3. The development of chemistries which selectively deposit on *GaAs* as opposed to *SiN*.
4. The development of an active sensor based control system to change process steps in real time.
5. Modifications of the reactor interior to reduce heavy metal impurities which presently may come from the microwave window holder and top flange of the chamber.
6. The implementation of liners with controllable temperature to modify the relative species concentrations and inhibit the consumption of atomic *F*.
7. The replacement of the quartz microwave window by a sapphire window to reduce the consumption of atomic *F*.

References

- ¹T. Ono, M. Oda, C. Takahashi, and S. Matsuo, *J. Vac. Sci. Technol. B* 4(3), 696, (1986).
- ²J. Asmussen, *J. Vac. Sci. Technol. A* 7 (3), 883, (1989).
- ³C. Constantine, D. Johnson, S. J. Pearton, U. K. Chakrabarti, A. B. Emerson, W. S. Hobson, And A. P. Kinsella, *J. Vac. Sci. Technol. B* 8 (4), 596, (1990).
- ⁴T. D. Mantei and T. E. Ryle, *J. Vac. Sci. Technol. B* 9(1), 29, (1991).
- ⁵J. Hommel, F. Schneider, M. Moser, C. Geng, F. Scholz and H. Schweizer, *Microelectronic Eng.* 23, 349 (1994).
- ⁶S. Samukawa, *J. Vac. Sci. Technol. B* 12 (1), 112 (1994).
- ⁷P. K. Gadgil, T. D. Mantei and X.C. Mu, *J. Vac. Sci. Technol. B* 12(1), 112 (1994).
- ⁸R. Cheung, Y. H. Lee, K. Y. Lee, T. P. Smith, III, D. P. Kren, S. P. Beaumont and C. D. W. Wilkinson, *J. Vac. Sci. Technol. B* 7 (6) 1462 (1989).
- ⁹T. Hara, J. Hiyoshi, H. Hamanaka, M. Sasaki, F. Kobayashi, K. Ukai, and T. Okada, *J. Appl. Phys.* 67 (6) 2836 (1990).
- ¹⁰K. K. Ko and S. W. Pang, *J. Electrochem. Soc.* 141 (1) 255 (1994).
- ¹¹K. L. Seaward, N. J. Moll, and W. F. Stickle, *J. Electrochem. Soc.* 137 (4), 385 (1990).
- ¹²S. W. Pang, *J. Electrochem. Soc.* 133 (4) 784 (1986).
- ¹³G. S. Oehrlein, Y. Zhang, O. Joubert, D. Vender, M. Haverlag, F. Bell and K. Kirmsel, *Tegal Symposium Proceedings*, 1993